J. Fluid Mech. (1992), *vol.* 238, *pp.* 221–250
Printed in Great Britain

Flow in a centrifugal spectrometer

By A. A. DAHLKILD[1], G. AMBERG[2] AND H. P. GREENSPAN[3]

[1] Department of Gasdynamics, Royal Institute of Technology, 100 44 Stockholm, Sweden

[2] Department of Hydrodynamics, Royal Institute of Technology, 100 44 Stockholm, Sweden

[3] Massachusetts Institute of Technology, Department of Mathematics, Cambridge, MA 02139, USA

(Received 1 August 1991 and in revised form 23 October 1991)

Rotational flow through narrow axial channels is considered in connection with a proposed technique to sort and separate particles according to sedimentation velocities. Nonlinear and linear axisymmetric flow through two channels connected by a slot in the vertical wall is studied numerically. A linearized formulation for the three-dimensional flow through a circumferentially blocked channel, with arbitrary positioning of the inlets and outlets, is examined analytically. Both approaches indicate that to have a sharp criterion for fractionation, the vertical shear layers on the channel walls must overlap. Otherwise, Coriolis effects, accompanying a strong azimuthal motion, make the sorting less precise. Results of an exploratory experiment with a simple two-stage machine demonstrate the feasibility of the basic process for simultaneous and continuous separation and fractionation.

1. Introduction

The centrifugal spectrometer (Greenspan 1989) is a device to separate and sort particles of different mass or size from a mixture in a truly continuous manner by means of a cascade through an internal nest of concentric, slotted cylinders, figure 1. (The fractionation of viral factors or latex beads are two of many possible applications.)

In a steady, axial, rotating flow of a mixture, various particle species will completely settle out of the stream at distinctly different distances along the channel length because the sedimentation time of a particle decreases with increasing mass or size. Of course, many old and new separation techniques are based on this observation. In the spectrometer, however, particles are also diverted to another channel at the appropriate position, either directly or by deflecting part of the flow. This enables the complete capture of the heaviest or largest particle species in the outer channel but only a fraction of any smaller component (assuming that all particles are heavier than the ambient fluid). By repeating this *cut* many times in the cylinder nest, in effect producing an internal cascade, the final result in a mixture of two particle sizes, for example, will be two purified streams each containing a single type. This concept extends easily to the simultaneous separation of several different particle groups.

Some of many designs and variations are shown in figure 1 in order to illustrate the fundamental principle. The bulk mixture in the geometry of figure 1 (*a*) contains rapidly and slowly sedimenting particles with the flow diverted three times in traversing the length of the centrifuge. The fluid moving in the different channels is collected and exits as two purified streams. If in general all the heavier particles, but

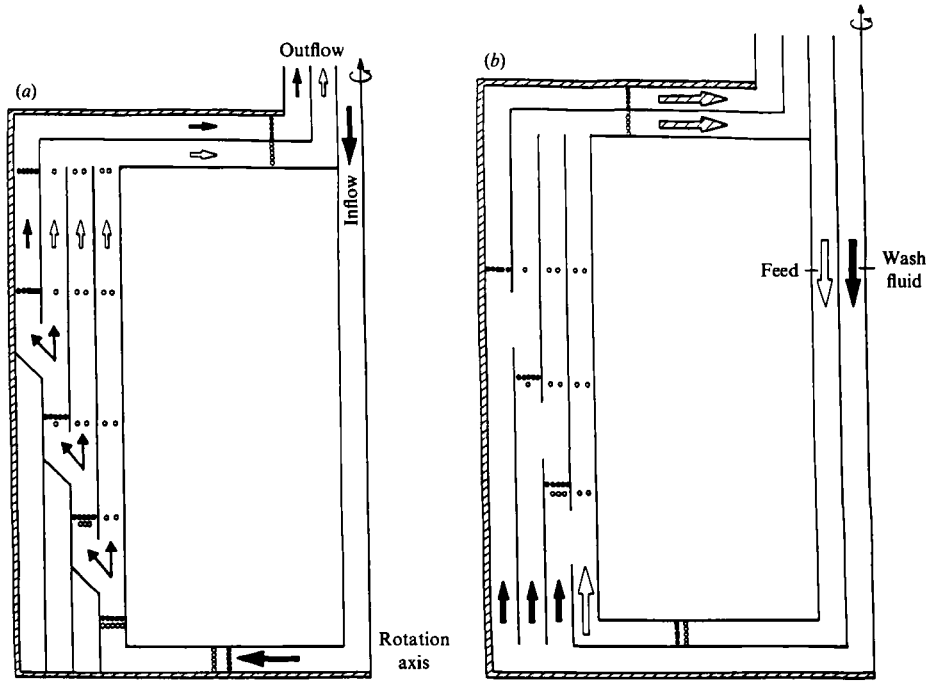

FIGURE 1. Two possible realizations of the basic fractionation concept. In (*a*) there is fluid between channels while in (*b*) only particles are so directed.

only a fraction, r say, of the lighter ones, are diverted at each stage, then after n cuts (30 or less in practice) the relative concentration of lighter to heavier particles in the outermost channel will be reduced by the factor r^n. In other words, a very high degree of purification can be attained.

Figure 1 (*b*) shows a design variation that utilizes a wash fluid channel so that only particles are transferred at each slot, in order to minimize complications arising from the outward flow in a rotating container. The apparatus may be completely sectioned into compartments by radial caulks in an effort to counteract the unwanted effects of the Coriolis force (Greenspan & Ungarish 1985; Amberg & Greenspan 1987, Shaflinger, Köppl & Filipczak 1986; Dahlkild & Greenspan 1989). Alternatively, it could be desirable to have a circumferential motion when the gap between cylinders is very small, in which case the complete radial barriers would be replaced by small spacers, the shape and positioning of which might also be used to alter the fluid flow beneficially.

The central problem concerns, then, axial flow in the very narrow vertical channels of a rotating container between which there is an exchange of particles and/or fluid. The approach here is three-fold: a numerical model for axisymmetric but nonlinear fluid motion; a linearized theoretical analysis to cover important non-symmetric configurations; and an exploratory experiment to demonstrate the feasibility of the basic concept, as well as to guide analytical formulations.

The non-dimensional problem for flow through rotating narrow axial channels is formulated first and specialized to the different geometries later.

Generally for the problems under study, the flow takes place in a narrow rotating cylindrical annulus centred around the axis of rotation as shown in figure 2. The mean radius is R' and an arclength of a possible compartment is $R'\Theta$. The channel

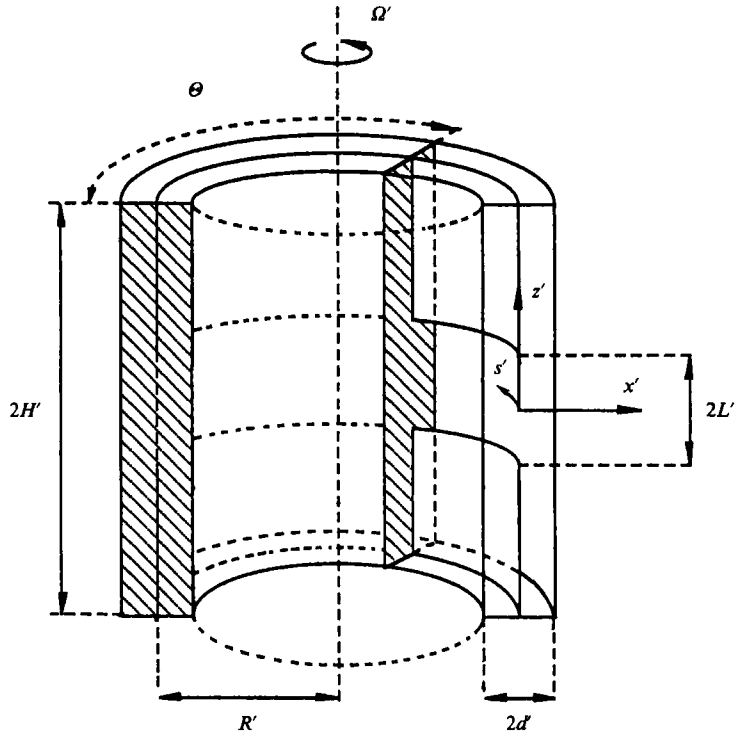

FIGURE 2. Sketch of cylindrical annulus with two narrow channels, and showing the coordinate system.

width is $2d'$ and the channel length, i.e. the height of the container, is $2H'$. The length of the slot connecting the two channels is $2L'$. We use a curvilinear coordinate system (x', s', z'), centred in the channel where the unit vectors $\boldsymbol{i}, \boldsymbol{j}$ and $\boldsymbol{k}$ are in the radial, angular and axial directions respectively. The axes are fixed in the container, rotating with angular velocity $\boldsymbol{k}\Omega'$. An incompressible Newtonian fluid of density ρ' and kinematic viscosity ν' is led through the container with specified inlet and outlet velocities. The velocity vector is denoted by

$$\boldsymbol{q}' = u'\boldsymbol{i} + v'\boldsymbol{j} + w'\boldsymbol{k}, \tag{1.1}$$

where u', v' and w' are the velocity components in the respective directions. A typical velocity is $V' = Q'/A'$, where Q' is the total volumetric throughput and A' is the area of the horizontal cross-section of one channel.

Non-dimensional, unprimed, variables are introduced using H', V' and $\rho'\Omega'H'V'$ as reference values for length, velocity and pressure, p', respectively. Since the channel is assumed to be narrow in the sense that $d' \ll R'$, the governing curvilinear equations are well approximated by their Cartesian counterparts. For conservation of volume and momentum this yields

$$\nabla \cdot \boldsymbol{q} = 0, \tag{1.2}$$

$$Ro\,\boldsymbol{q} \cdot \nabla \boldsymbol{q} + 2\boldsymbol{k} \times \boldsymbol{q} = -\nabla P + E\nabla^2 \boldsymbol{q}, \tag{1.3}$$

where $P = p - \rho'\Omega'^2(R'+x')^2/(2\rho'\Omega'H'V')$ is the non-dimensional reduced pressure, $E = \nu'/(\Omega'H'^2)$ is the Ekman number, and $Ro = V'/(\Omega'H')$ is the Rossby number. No-slip conditions for the fluid velocity are imposed on all boundaries and the velocity component normal to the wall is prescribed at the inlets and outlets.

A sedimenting particle is assumed to undergo a quasi-steady motion in which the centrifugal force is balanced by viscous drag. In the limit of a dilute suspension of non-interacting spherical particles of radii $a'_p \ll d'$ and density ρ'_p, a Stokesian drag $6\pi\rho'\nu' a'_p(\boldsymbol{q}'_p - \boldsymbol{q}')$ and an effective centrifugal force $\frac{4}{3}\pi a'^3_p(\rho'_p - \rho')\,\Omega'^2(R' + x')\,\boldsymbol{i}$, give the non-dimensional particle velocity as

$$\boldsymbol{q}_p = \boldsymbol{q} + \frac{\epsilon\beta}{Ro}(R + x)\,\boldsymbol{i}, \tag{1.4}$$

where the non-dimensional numbers

$$\epsilon = \frac{\rho'_p - \rho'}{\rho'}, \quad \beta = \frac{2}{9}\frac{a'^2_p}{\nu'/\Omega'}, \tag{1.5a, b}$$

are referred to as the relative density difference and particle Taylor number respectively. As $d' \ll R'$, the particle settling velocity $U_s = (\boldsymbol{q}_p - \boldsymbol{q})\cdot\boldsymbol{i}$, varies only slightly in the channel and is, for simplicity, assumed to be constant in the computations:

$$U_s = \frac{\epsilon\beta}{Ro}R. \tag{1.6}$$

In accordance with the dilute-limit approximation, the fluid velocity $\boldsymbol{q}$ is calculated from the single-phase equations formulated above and particles with a given, well-defined settling velocity are then traced through the container. Particles that have settled gainst the wall are assumed to slip or roll along the wall in the direction of the local wall shear stress of the single-phase flow. Gravity, which easily can be accounted for in (1.6), is neglected here owing to the rapid rotation of the container ($g' \ll \Omega'^2 R'$).

An important concept is this context is the critical settling velocity, U'_{cr} say, i.e. the lowest particle settling velocity for which all particles of a given size are diverted to the outer channel. An accurate estimate of this may be obtained from simple kinematic arguments. Let Q'_i be the total volume flux (per unit length in the azimuthal direction) at the input end of the inner channel, from which particles are diverted. Let $(1-\gamma)$ be the fraction of this flow rate that is deflected through the slot to the outer channel. Then if the radial particle settling velocity is assumed to be $U'_s \leqslant U'_{cr}$, the volumetric flow of settling particles into the lower part of the dividing wall (see figure 2), from a suspension with uniform particle volume fraction α, is $\alpha U'_s(H' - L')\,2\pi R'$. The volumetric flow of particles into the slot is

$$(\alpha Q'_i(1-\gamma) + \alpha U'_s\,2L')\,2\pi R'.$$

The total loss of particles from the flow in the inner channel up to the downstream edge of the slot (per unit length in the azimuthal direction) is then

$$Q'_p = \alpha(H' + L')\,U'_s + \alpha Q'_i(1-\gamma). \tag{1.7}$$

We now define the critical minimum settling velocity at which particles are completely diverted into the outer channel. This is obtained from (1.7) by requiring that the total loss of particles from the flow in the inner channel up to the downstream edge of the slot equals the total input volumetric flow rate of particles, $Q'_p = \alpha Q'_i$. Thus

$$U'_{cr} = \gamma\frac{Q'_i}{H' + L'}. \tag{1.8a}$$

In non-dimensional form this relation reads

$$U_{\rm cr} = \gamma \frac{Q_{\rm i}}{1+L}. \tag{1.8b}$$

In place of γ, $U_{\rm cr}$ could be regarded as one of the non-dimensional parameters specifying the problem.

For particles with a smaller settling velocity than the critical one, $U'_{\rm s} < U'_{\rm cr}$, only a fraction, r say, of the total input volumetric flow rate of particles is diverted to the outer channel. hence, $Q'_{\rm p} = r\alpha Q'_{\rm i}$ and (1.7) with (1.8a) then give

$$r = 1-\gamma\left(1-\frac{U'_{\rm s}}{U'_{\rm cr}}\right). \tag{1.9}$$

2. Axisymmetric flow

In order to investigate details of the flow through the slot, we have made two-dimensional computations using the full Navier–Stokes equations in a geometry with two axial channels connected by a slot in the dividing wall between them. The main simplification is the assumption of axial symmetry (all quantities are independent of the azimuthal coordinate), which is not quite true in the experiments nor in the actual device. However, these computations capture the complicated flow patterns around the sharp edges of the slot, which could be unfavourable for separation.

2.1. *Formulation*

The computations were done using a program, devised by G. Amberg & M. Ungarish as part of their ongoing research, for solving the Navier–Stokes equations in a rotating frame of reference. This program was modified to include a dividing wall separating two axial channels, with a connecting slot in this wall through which fluid is diverted from one channel to the other. The formulation of non-dimensional equations is as in §1, except that here it is also assumed that all quantities are independent of the azimuthal coordinate. As discussed in §1, the channel is assumed to be narrow in the sense that its width is small compared to the radial distance to the axis of rotation. It is then possible to use Cartesian coordinates, as in (1.2) and (1.3).

The basic equations were solved numerically; the computations are time dependent, even though the results reported here are all steady. In order to reach a steady state, the computations were run long enough for transients to decay. The code uses a finite-difference discretization on a staggered grid. The incompressibility condition is satisfied by using a scheme of the pressure correction type, similar to that used by van Kan (1986). Both viscous and Coriolis terms are treated implicitly. At each time step, a set of linear equations similar to the Poisson equation must be solved, and this is done iteratively by the conjugate gradient method. Convective terms are treated by explicit upstream differencing, as described by Davis & Moore (1982). The resulting stability restriction on time step is the usual Courant number inequality, $U < \Delta x/\Delta t$. The implicit treatment of the Coriolis term removes the restriction $\Delta t < 1/\Omega$, which would prevail if the Coriolis term was explicit. However, it is often necessary to keep $\Delta t \approx 1/\Omega$, if an accurate time dependence is required. The numerical procedure will be described in more detail in a future publication by G. Amberg & M. Ungarish. The dividing wall was introduced in the simplest possible fashion, letting it occupy a width of two cells in the staggered grid. The

implementation of boundary conditions (zero tangential and normal velocity) on the dividing wall is then straightforward.

The geometry used in the computations is shown in figure 2. Inflow and outflow may be specified at either of the ends of the channels. To investigate basic properties of the flow, the symmetric case where fluid is fed in at the bottom of the inner channel, and withdrawn at the upper end of the outer channel, was studied. In order to imitate the actual device (see figure 1), another case where half the flux is diverted was studied. The flow is then introduced at the bottom end of the inner channel and withdrawn at the top of the inner and outer channels, at equal rates. Thirdly, a different mode of operation was simulated, in which no flux is diverted. Equal flow rates are prescribed at the bottom and taken out at the top of each channel; the velocity profiles prescribed at inflow and outflow are parabolic. In all cases considered here, the slot was placed symmetrically around the mid-height and the channels were of equal thickness.

In this paper only particles that are heavier than the fluid are considered, in which case settling is outward. The case with light particles settling inward, when the inflow is at the bottom of the outer channel, is completely analogous within the present formulation.

2.2. *Results*

To investigate the flow in the vicinity of the slot we have made simulations of a few basic cases. First we have looked at a symmetric configuration where the entire mass flux is diverted from the inner to the outer channel. Runs were made at different Rossby numbers to examine the effect of nonlinearity. Secondly we have made simulations that are relevant for the actual separation device, using the same parameter values as in the experiments discussed later. These parameters have also been varied to show how a change in the operation of the centrifuge modifies the flow. Thirdly the paths of sedimenting particles in the flow field were traced to investigate separation. Since the device is intended for use at low volume fraction we have traced single particles, without considering particle interaction effects.

In the case where all the mass flux is diverted from the inner to the outer channel, we used two different values of the Rossby number: first $Ro = 8 \times 10^{-4}$, corresponding to a fairly weak flow. The Ekman number was $E = 1.6 \times 10^{-3}$ and the width of one channel was $d = 0.284$ (corresponding to $d' = 0.284H'$). The resulting flow field after a steady state is reached is shown in figure 3. Velocity arrows in the (x, z)-plane are shown in figure 3 (*a*), and levels of constant azimuthal velocity v are shown in figure 3 (*b*). There is a clear symmetry between the inflow and outflow sides. The azimuthal velocity v is a maximum in the slot gap, as is the radial velocity u. The azimuthal velocity is fairly independent of z except near the edges of the slot. This is because the channel width has been chosen to be the same order of magnitude as the $E^{\frac{1}{3}}$-layers that would be expected in a wider channel, $d = 0.284$, which should be compared to $E^{\frac{1}{3}} = 0.117$. Also note that there are weak currents that penetrate into the dead-end sections of the channels. Following the flow from inlet, the velocity profile is concentrated towards the dividing wall as the slot is approached. At the slot edge, half the flow turns round the edge and continues in the opposite direction on the other side of wall. The remaining half of the flow detours into the dead-end part of the channel and eventually turns round the opposite slot edge, to continue toward the outlet. The flow around the slot edges is quite intense and is concentrated into two jets, one at each edge. We have not tried to do a careful estimate of the width (in the z-direction) of these jets, but from basic theoretical considerations it seems likely that it would be $E^{\frac{1}{3}}$.

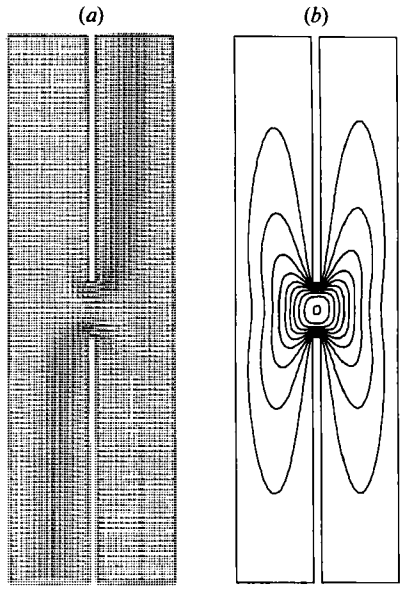

FIGURE 3.

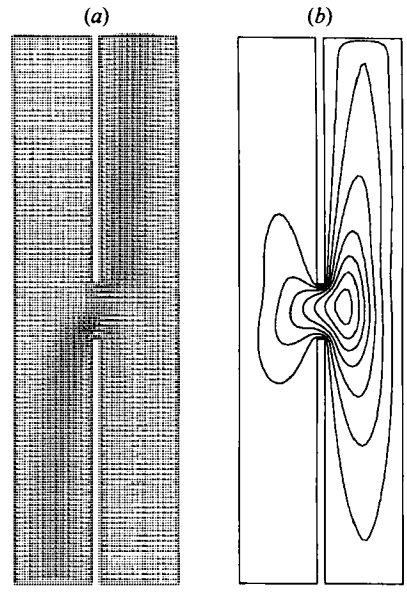

FIGURE 4.

FIGURE 3. Linear flow regime when the entire volume flux is diverted through the slot showing (*a*) velocity arrows in the (x, z)-plane and (*b*) levels of constant azimuthal velocity: $v = -6.88 + 0.625i$, $i = 1, 2, \ldots, 10$. $E = 1.6 \times 10^{-3}$, $Ro = 8 \times 10^{-4}$.

FIGURE 4. Nonlinear flow regime when the entire volume flux is diverted through the slot showing (*a*) velocity arrows in the (x, z)-plane and (*b*) levels of constant azimuthal velocity: $v = 4.58 + 0.417i$, $i = 1, 2, \ldots, 11$. $E = 1.6 \times 10^{-3}$, $Ro = 8 \times 10^{-2}$.

To see the nonlinear effects, we also computed a case corresponding to a larger flow rate, corresponding to $Ro = 8 \times 10^{-2}$, keeping all other parameters the same as in figure 3. The most striking feature of the flow field, shown in figure 4, is that the symmetry is broken. The maximal azimuthal velocity is now displaced outwards, out of the slot gap, by convection of v, clearly showing the importance of nonlinearity. The swirl is decreased on the upstream side, and intensified on the downstream side, where it also penetrates deeper into the dead-end part of the channel. Also more than half the flow now turns round the lower, upstream edge of the slot. Consequently, the current penetrating into the upper end of the inner channel, which feeds the flow around the other edge, is weaker. The importance of nonlinearity may be estimated from the momentum equation (1,4). Given that the lengthscale in the radial direction is given by the channel width to be of order $E^{\frac{1}{3}}$, order of magnitude estimates imply that the nonlinear term in the momentum equation is of importance if $Ro \geqslant E^{\frac{1}{3}}$. This result may also be inferred from the results of Barcilon & Berg (1971). Numbers here give $Ro/E^{\frac{1}{3}} = 0.68 \approx 1$, while for the case shown in figure 3, $Ro/E^{\frac{1}{3}} = 6.8 \times 10^{-3} < 1$.

In order to investigate the actual device, a case similar to the experiment to be presented in §4 was simulated, figure 5. Comparing figure 2, showing the geometry in the computation, and figure 1, showing the actual device, the major difference is that the closed bottom part of the outer channel is blocked just above the slot in figure 1, while in the computation, this channel end was instead sealed at the bottom. This channel end appears to be rather passive, and we do not believe that it is misleading to use the geometry in figure 2 instead of that in figure 1. The parameter values for this case were $E = 1 \times 10^{-4}$, $Ro = 6.42 \times 10^{-4}$. The typical length was equal to the

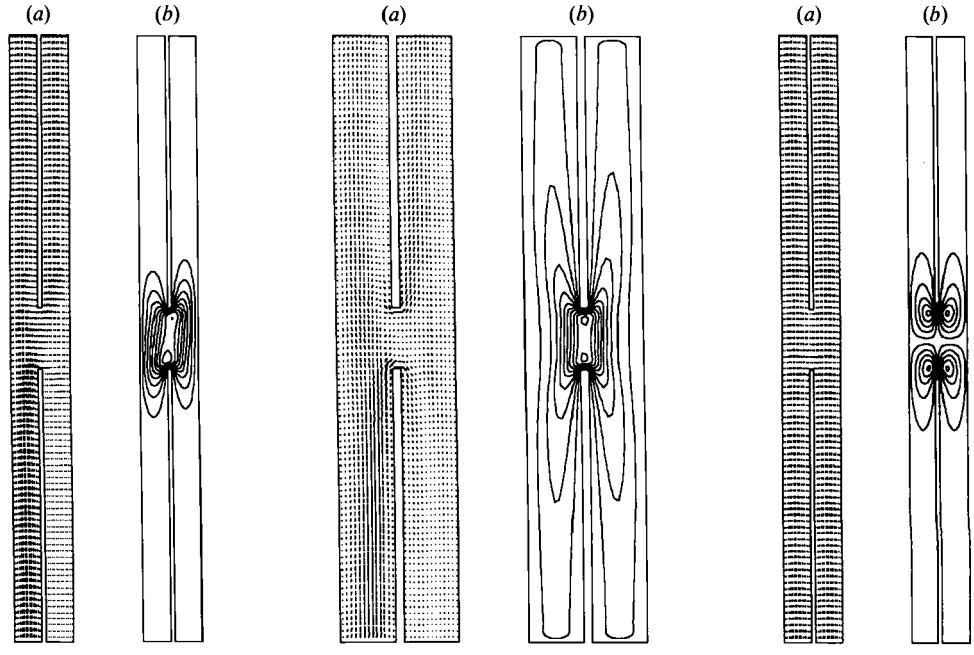

FIGURE 5. FIGURE 6. FIGURE 7.

FIGURE 5. Simulation of experiment where half the flux is diverted through the slot showing (*a*) velocity arrows in the (x,z)-plane and (*b*) levels of constant azimuthal velocity: $v = -2.29+0.208i$, $i = 1,2,\ldots,9$. $E = 1\times10^{-4}$, $Ro = 6.42\times10^{-4}$, $L = 0.065$, $d/E^{\frac{1}{3}} = 1.28$.

FIGURE 6. Flow regime with separated shear layers when half the flux is diverted through the slot showing (*a*) velocity arrows in the (x,z)-plane and (*b*) levels of constant azimuthal velocity: $v = -4.58+0.417i$, $i = 1,2,\ldots,10$. $E = 1\times10^{-4}$, $Ro = 6.42\times10^{-4}$, $L = 0.065$, $d/E^{\frac{1}{3}} = 2.54$

FIGURE 7. Simulation of wash fluid case where no flux is diverted through the slot showing (*a*) velocity arrows in the (x,z)-plane and (*b*) levels of constant azimuthal velocity: $v = -0.25+0.045i$, $i = 1,2,\ldots,10$. $E = 1\times10^{-4}$, $Ro = 6.42\times10^{-4}$, $L = 0.065$, $d/E^{\frac{1}{3}} = 1.28$.

channel height in the experiment, while the computational domain was somewhat smaller, so that the non-dimensional half-length of the channels is 0.65 in the simulations. The non-dimensional width of each channel is $d = 0.059$, which again means that the channel width is the same order of magnitude as a $\frac{1}{3}$-power layer ($E^{\frac{1}{3}} = 0.046$). The ratio $Ro/E^{\frac{1}{3}} = 1.4\times10^{-2}$ indicates that the flow is fairly linear.

In the computation in figure 5, the height of the slot and the channel length from inlet (bottom) to the slot was the same as in the experiment. The channel length downstream of the slot was greater in the experiment, but since the velocity profile becomes fully developed and independent of the axial coordinate this should not be important within the computed length. Figure 5 shows computed results after a steady state has been attained: velocity arrows in the (x,z)-plane are shown in figure 5(*a*), and contours of constant azimuthal velocity in figure 5(*b*). The mass flux enters at the bottom of the left (inner) channel and is withdrawn at the tops of each of the two channels. Here the channel is narrower than in figures 3 and 4; $d/E^{\frac{1}{3}} = 1.28$, whereas it was 2.43 above. As a consequence, the flow in the channels away from the slot is less modified by rotation: the azimuthal velocity is again maximal in the slot, but it decays within less than one slot height away from the slot. As soon as the azimuthal velocity has vanished, the velocity profiles in each channel are parabolic,

just as they would be in a non-rotating frame of reference. The radial transport in Ekman layers at the channel ends that would dominate the flow in ordinary linear rotating flow is here suppressed by the close spacing of the vertical walls. The velocity profiles away from the slot area are also independent of the axial variable, and the flow around the slot will be unaffected by conditions at the outflow. It is still important to keep the length from the inlet to the slot correct, since we wish to predict trajectories of settling particles that enter at the inlet. The flow around the slot shows many similarities with the case in figure 3. The flow is apparently linear, with the maximum azimuthal velocity centred in the slot. The radial flow is concentrated around the slot edges. There is a current that penetrates into the dead-end lower part of the outer channel, but here it reaches less than one slot height below the slot.

One other case was tried to see how modifications of the channel width affects the flow. The same parameter values as in figure 5 were used, except that the non-dimensional channel with d was increased to 0.118, making $d/E^{\frac{1}{3}} = 2.54$. Figure 6 shows velocity arrows in the (x, z)-plane and levels of azimuthal velocity. Comparing to figure 5, the most apparent difference is that the region of non-zero azimuthal velocity around the slot now extends further away from the slot, as far as the channel ends. The modifications of the flow pattern in the (x, z)-plane also extends further from the slot. In particular, looking at the left (inner) downstream edge of the slot, there is evidence of a flow reversal along the wall, just above the slot. The axial velocity is actually directed downwards, against the overall flow direction, in a region extending from the slot to a stagnation point located at about $z = 0.308$ ($z = 0$ at the centre of the slot and 0.65 at the top). This is because the radial jet around the edge will be quite intense (no doubt some sort of singularity in a linear asymptotic theory for small Ekman numbers) and close to the edge this 'singularity' may then dominate the basic flow. This flow reversal may be quite harmful for the operation of the device.

One way of removing the harmful flow around the slot edges would be to allow the fluid to pass by the slot, without any net volumetric flow rate through the slot. Fluid is then introduced and withdrawn at equal rates at the bottom and top of each channel. A computation was done with the same geometry and parameter values as in the case presented in figure 5, but with the inflow distributed equally between the two channels. The velocity field is shown in figure 7. The axial velocity shows Poiseuille profiles which do not completely merge at the slot. The azimuthal velocity shows four lobes around the slot edges. These are much weaker than in the case in figure 5; the azimuthal velocity in figure 7(*b*) is approximately 10% of that in figure 5(*b*). More importantly, there is no trace of a flow reversal in the axial flow past the slot.

In order to investigate sorting by settling velocity, we have traced trajectories of single settling particles, to see whether they are caught in the outer channel. Particles have been traced from different positions along the inlet through the device. Figure 8(*a*) shows paths of particles entering at the lower inner inlet for the case presented in figure 5, fairly narrow channels with a net flow through the slot. The particles have a critical settling size according to (1.8), which gives a value of $U_s = 0.04119$ here. The last particle entering at the innermost location at the lower end of the inner channel hits the downstream edge of the slot exactly. In the case presented in figure 5 there is flow reversal above the slot, quite close to the edge. The dashed line shows a trajectory corresponding to a settling velocity of $U_s = 0.0398$, 3.5% lower than the theoretical. This particle settles on the dividing wall above the slot, at a location

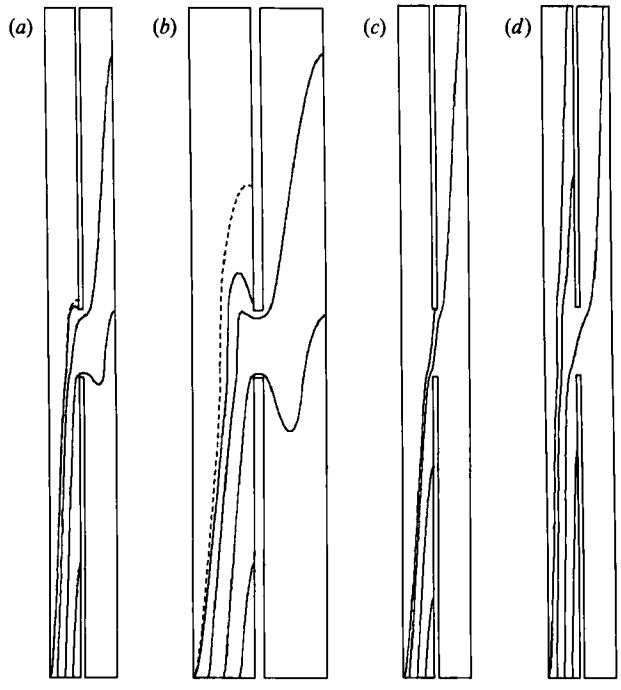

FIGURE 8. Calculated paths of sedimenting particles entering at the inlet. (*a*, *b*) The cases shown in figures 5 and 6 respectively. Full lines denote particles with (*a*) $U_s = 0.0412$, (*b*) $U_s = 0.0824$, the minimum settling velocity for which all particles pass through the slot according to the theoretical estimate. The dashed line denotes particles with (*a*) $U_s = 0.0398$, (*b*) $U_s = 0.0613$, the true minimum settling velocity, taking into account the flow reversal above the slot. (*c*) The wash fluid case in figure 7; $U_s = 0.0412$ according to the theoretical estimate. (*d*) The same case as in figure 5; $U_s = 0.0206$, half the critical settling velocity according to the theoretical estimate.

where the wall shear changes sign from downwards below, to upwards above. This then represents the limiting settling velocity; particles settling more slowly will settle above the stagnation point where the flow velocity will drag them upwards, particles settling faster will settle below the stagnation point where the flow velocity will drag them down into the slot and the outer channel. Since the flow reversal is weak, the critical settling velocity differs only slightly from that given by (1.8).

Figure 8 (*b*) shows particle paths for the flow in the wider channel, which display a significant region of flow reversal above the slot. The idea for the sorting is that particles settling fast enough, so that they have traversed the channel width by the time they reach the upper edge of the slot, will appear in the outer channel only. The formula for the settling velocity required for a particle to be captured, (1.8), derived in the introduction, is based on kinematic considerations only and does not depend strongly on the peculiarities of the flow field. This formula is true under the assumption that particles settling into the dividing wall above the slot (downstream) will be dragged upwards, away from the slot. When a flow reversal appears, the shear stress on the wall will instead be directed down towards the slot in the region from the upper edge of the slot to the stagnation point above. The upper end of the length available for settling of particles that are diverted to the outer channel is thus extended from the upper slot edge to the stagnation point above. Smaller particles than expected may then be entrained into the outer channel. This phenomenon makes the selection of particles less precise, and should be avoided.

The full lines in figure 8(*b*) correspond to particles with a settling velocity computed from (1.8) which gives 0.08238 for this case; these are all diverted into the outer channel. The trajectory of the particle coming from the lower inner corner makes an excursion above the slot in the inner channel, before it settles on the dividing wall just above the slot edge. The shear stress on the wall will drag this particle down into the slot. The dashed line shows the trajectory for a particle with a settling velocity of 0.0613. In figure 6, the location of the stagnation point on the inner side of the sidewall above the slot may be estimated to be at a position $z = 0.308$, i.e. at a distance of 0.24 above the slot edge. The settling velocity 0.0613 has been obtained from the kinematic argument in the introduction, replacing the length over which particles that are diverted settle, $H'+L'$, by $H'+L'+0.24H'$, the distance from the inlet to the upper slot edge plus the length of the flow reversal region on the upper sidewall. This trajectory is seen to hit the sidewall precisely at the stagnation point. All particles with greater settling velocities will hit the dividing wall below the stagnation point, where the viscous stresses will drag them downwards and into the slot. Thus the limit on settling velocity for particles that are diverted into the outer channel has decreased by 25% from that given by (1.8).

In figure 8(*c*) particle trajectories for the case in figure 7 with no net flow through the slot are shown. The particle settling velocity is chosen to be the critical one according to (1.8). The trajectory of the innermost particle is seen to hit the upper slot edge head on. In this case there is no trace of a flow reversal, because of the absence of a net volume flux through the slot and the sorting is expected to be very precise. The wash fluid mode of operation thus removes this complication, and should be beneficial for separation. The throughput rate for a given critical particle settling velocity is however lower for the wash fluid mode than for a case with diversion of flow to the outer channel.

Figure 8(*d*) shows trajectories for particles with half the critical settling velocity, i.e. the lighter or smaller species that is to be removed from the stream passing through the slot. They are drawn for the case in figure 5, with a narrow channel width and half the flow rate passing through the slot. The particle entering at the centre of the inner bottom end is seen to pass through the slot. Equation (1.9) shows that $\frac{1}{4}$ of the smaller particles are removed from the stream passing through the slot. Since this cut is to be repeated many times this is however quite sufficient. For example, the number of small particles in the stream is reduced by a factor 0.75 at each cut, giving only $0.75^{10} = 5.6\%$ of the small particles left after ten cuts.

As noted above, the importance of the Coriolis force increases with increasing channel width and the flow in figure 6 shows more of the characteristics of a rotating flow than that in figure 5. In industrial centrifuges it is important to counteract the effects of the Coriolis force, in order to obtain good separative performance. That is often done by using radial channels that are narrow in the sense that their thickness is the order of the Ekman-layer thickness. Here, with axial channels, the relevant channel width is instead the thinnest of the vertical boundary layers, $E^{\frac{1}{3}}$. The particle trajectories in figure 8(*b*), as discussed above, show that indeed it is important to subdue the Coriolis force for successful operation of this device also.

3. Three-dimensional flow

We now drop the assumption of axial symmetry in order to investigate possible changes in the performance of a circumferentially blocked apparatus (see figure 2). The linearized formulation also allows arbitrary positioning of the inlets and outlets,

but the meridional barriers are assumed to be impenetrable. Only a single channel without internal boundaries is considered, for which a rather straightforward analytical approach is possible in the linear regime. This means that at best an imitation of the flow in the spectroscope can only be achieved from this model by introducing an outlet in the form of a horizontal slot in the outer vertical wall where velocities are prescribed. The complete flow through a slot is a far more difficult problem.

3.1. *Formulation*

We study here the flow due to a source–sink distribution on the boundary of a channel with meridional barriers positioned at $s = \pm R\Theta$. An asymptotic solution is sought to the boundary-value problem (1.2), (1.3) as formulated in §1 for $E \ll 1$, $Ro \ll 1$. The channel width is assumed to be of order $H'E^{\frac{1}{3}}$ so that

$$a = d'/(H'E^{\frac{1}{3}}) \tag{3.1}$$

is an order-one quantity. A new, stretched coordinate is therefore introduced:

$$\xi = x/E^{\frac{1}{3}}. \tag{3.2}$$

The non-dimensional domain for the flow is then

$$|\xi| \leqslant a; \quad |s| \leqslant R\Theta; \quad |z| \leqslant 1. \tag{3.3}$$

The boundary conditions on the barriers and on the other vertical walls are

$$\boldsymbol{q}(s = \pm R\Theta) = 0, \tag{3.4}$$

$$u(\xi = \pm a) = E^{\frac{1}{3}} U_{\pm}(s, z), \tag{3.5a}$$

$$v(\xi = \pm a) = w(\xi = \pm a) = 0 \tag{3.5b, c}$$

by which global conservation of volume yields

$$\int_{-R\Theta}^{R\Theta} \mathrm{d}s \int_{-1}^{1} [U_+(s,z) - U_-(s,z)]\,\mathrm{d}z + \int_{-a}^{a} [W_+(\xi,s) - W_-(\xi,s)]\,\mathrm{d}\xi = 0, \tag{3.6}$$

where $W_{\pm}$ are the specified normal velocity components at the horizontal top and bottom boundaries. The weak radial velocity at $\xi = \pm a$, which has been introduced to allow simulation of a flow partly deflected radially through a slot in the vertical wall is thus taken to be of the same order of magnitude, $\sim E^{\frac{1}{3}}$, as the net vertical transport over the horizontal boundaries. It turns out that this also validates the scaling of v and w.

For small Ekman numbers large forces due to horizontal shear are restricted to thin Ekman layers close to the non-vertical walls, and the problem is simplified by using the equivalent linear Ekman-layer compatibility conditions at the horizontal endwalls for the interior flow (Greenspan 1968, p. 92). In terms of the stretched variable ξ they are

$$w(z = \pm 1) = \mp \frac{E^{\frac{1}{3}}}{2} \left[\frac{\partial v}{\partial \xi} - E^{\frac{1}{3}} \frac{\partial u}{\partial s} \right]_{z = \pm 1} + W_{\pm}(\xi, s). \tag{3.7a, b}$$

For the interior flow then, no-slip conditions at these walls are dropped together with terms of vertical diffusion in the momentum equations. The Rossby number is

assumed small enough to allow a linear analysis (see §3.2) and the governing equations then reduce to

$$\frac{\partial u}{\partial \xi}+E^{\frac{1}{3}}\frac{\partial v}{\partial s}+E^{\frac{1}{3}}\frac{\partial w}{\partial z}=0, \tag{3.8}$$

$$2\boldsymbol{k}\times\boldsymbol{q}_{\mathrm{h}}=-\nabla_{\mathrm{h}}\bar{P}+E^{\frac{1}{3}}\nabla_{\mathrm{h}}^{2}\boldsymbol{q}_{\mathrm{h}}, \tag{3.9a}$$

$$0=-\frac{\partial \bar{P}}{\partial z}+\nabla_{\mathrm{h}}^{2}w, \tag{3.9b}$$

where $\bar{P}=P/E^{\frac{1}{3}}$ is the rescaled pressure, $\boldsymbol{q}_{\mathrm{h}}=\boldsymbol{q}-\boldsymbol{k}w$ is the horizontally projected velocity vector and

$$\nabla_{\mathrm{h}}=\left(\frac{\partial}{\partial \xi},E^{\frac{1}{3}}\frac{\partial}{\partial s},0\right). \tag{3.10}$$

The boundary-value problem is conveniently formulated in terms of the pressure, $\bar{P}$, for which it is well known (Greenspan 1968, p. 29) that a single equation can be derived. It follows from (3.8) and (3.9) that

$$\nabla_{\mathrm{h}}^{6}\bar{P}+4\frac{\partial^{2}\bar{P}}{\partial z^{2}}+\left(E^{\frac{2}{3}}\frac{\partial^{2}}{\partial z^{2}}(\nabla_{\mathrm{h}}^{4}\bar{P})\right)=0. \tag{3.11}$$

Since E, by assumption, is small we shall neglect the last term in (3.11). The velocity components are given by

$$u=E^{\frac{1}{3}}\left(-\frac{1}{2}\frac{\partial \bar{P}}{\partial s}+\frac{1}{4}\frac{\partial}{\partial \xi}\nabla_{\mathrm{h}}^{2}\bar{P}\right),\quad v=\frac{1}{2}\frac{\partial \bar{P}}{\partial \xi},\quad \frac{\partial w}{\partial z}=-\tfrac{1}{4}\nabla_{\mathrm{h}}^{4}\bar{P}, \tag{3.12a–c}$$

where only the leading-order terms in the Ekman number are kept. In terms of the pressure, the boundary conditions (3.4) and (3.5) with (3.12) give

$$-\frac{1}{2}\frac{\partial \bar{P}}{\partial s}+\frac{1}{4}\frac{\partial}{\partial \xi}\nabla_{\mathrm{h}}^{2}\bar{P}=U_{\pm}(s,z)\quad\text{at}\quad \xi=\pm a, \tag{3.13a}$$

$$\frac{\partial \bar{P}}{\partial \xi}=\nabla_{\mathrm{h}}^{4}\bar{P}=0\quad\text{at}\quad \xi=\pm a, \tag{3.13b, c}$$

$$\frac{\partial \bar{P}}{\partial s}=\frac{\partial \bar{P}}{\partial \xi}=\frac{\partial^{4}\bar{P}}{\partial s^{4}}=0\quad\text{at}\quad s=\pm R\Theta \tag{3.14a–c}$$

and (3.7) with (3.9*b*) and (3.12*a*, *b*) yield, to leading orders,

$$\frac{\partial \bar{P}}{\partial z}\pm\frac{E^{\frac{1}{3}}}{4}\nabla_{\mathrm{h}}^{2}\bar{P}=\nabla_{\mathrm{h}}^{2}W_{\pm}(\xi,s)\quad\text{at}\quad z=\pm 1, \tag{3.15}$$

which completes the formulation of the boundary-value problem for $\bar{P}$.

3.2. *Analysis*

Meridional boundary layers of thickness $O(E^{\frac{1}{3}})$ are expected adjacent to the barriers at $s=\pm R\Theta$. It follows from (3.11) and (3.12) that outside these boundary layers $u\sim E^{\frac{1}{3}}$ whereas v, w, and $\bar{P}$ are all $O(1)$. Inside the boundary layers, where

$s = \pm R\Theta + O(E^{\frac{1}{3}})$, we have $u \sim v \sim w \sim \bar{P} \sim 1$. The horizontal force balance is here approximately geostrophic so that the pressure in each horizontal cut acts as a stream function for u and v to lowest order. An order of magnitude analysis shows that a linear analysis in these layers is justified if $Ro \ll E^{\frac{2}{3}}$. For $Ro \sim E^{\frac{2}{3}}$ the main horizontal force balance is still geostrophic but convection and diffusion of vorticity are nevertheless of comparable magnitudes. In the interior, where the appropriate lengthscale in the flow direction is much larger, the constraint on the Rossby number is relaxed to $Ro \ll E^{\frac{1}{3}}$, see Barcilon & Berg (1971), according to which a linear analysis for axisymmetric flow is justified if $V'/\Omega' d' \ll 1$. In terms of Ro and E this is equivalent to $RoE^{-\frac{1}{3}} \ll 1$, which also holds in the non-axisymmetric case studied here.

Here only the interior flow outside the barrier boundary layers is considered. The equation for $\bar{P}$ is thus approximated with the standard Stewartson $E^{\frac{1}{3}}$-layer equation

$$\frac{\partial^6 \bar{P}}{\partial \xi^6} + 4\frac{\partial^2 \bar{P}}{\partial z^2} = 0, \tag{3.16}$$

and (3.12a, c) are simplified to

$$u = E^{\frac{1}{3}}\left(-\frac{1}{2}\frac{\partial \bar{P}}{\partial s} + \frac{1}{4}\frac{\partial^3 \bar{P}}{\partial \xi^3}\right), \quad \frac{\partial w}{\partial z} = -\frac{1}{4}\frac{\partial^4 \bar{P}}{\partial \xi^4}. \tag{3.17a, b}$$

Since for the interior flow $u \sim E^{\frac{1}{3}}$ we define

$$\bar{u} = u/E^{\frac{1}{3}}, \tag{3.18}$$

whereas for v (3.12b) still holds. Of the boundary conditions at $\xi = \pm a$, (3.13a, c) are approximated by

$$\frac{1}{2}\frac{\partial \bar{P}}{\partial s} + \frac{1}{4}\frac{\partial^3 \bar{P}}{\partial \xi^3} = U_{\pm}(s, z), \quad \frac{\partial^4 \bar{P}}{\partial \xi^4} = 0. \tag{3.19a, b}$$

At the radial barriers, the interior solution cannot satisfy either the no-slip or the non-penetrating conditions, which have to be replaced by integral constraints. Since the flow is completely blocked by the barriers and since the boundary layers adjacent to the barriers can support at the most a vertical volume flux of order $E^{\frac{2}{3}}$ as $w \sim 1$, the net interior flow in the azimuthal direction, which is $O(E^{\frac{1}{3}})$, must be zero at every vertical position of the barrier. This yields

$$\int_{-a}^{a} v(\xi, \pm R\Theta, z)\,\mathrm{d}\xi = \tfrac{1}{2}[\bar{P}(a, \pm R\Theta, z) - \bar{P}(-a, \pm R\Theta, z)] = 0, \tag{3.20}$$

for all values of z, and this replaces (3.14) for the interior flow. For the conditions at the horizontal boundaries, all derivatives with respect to s are dropped accordingly and for simplicity we also neglect the Ekman-layer suction which is of order $E^{\frac{1}{3}} \ll 1$. We then have

$$\frac{\partial \bar{P}}{\partial z}(z = \pm 1) = \frac{\partial^2 W_{\pm}}{\partial \xi^2}(\xi, s), \tag{3.21a, b}$$

$$w(z = \pm 1) = W_{\pm}(\xi, s) \tag{3.22a, b}$$

for the interior flow at the top and bottom walls. Formally, then, to obtain $\bar{u}$, v, and w we first solve for $\bar{P}$ from (3.16) with (3.13b), (3.19), (3.20) and (3.21). The horizontal velocity components then follow directly from (3.12b) and (3.17a), whereas w is integrated from (3.17b) with either of (3.22a, b).

The solution of the problem is obtained as a superposition of two parts, each consisting of very complex series of eigenfunctions. An outline of the procedure is presented in the Appendix and more details will appear elsewhere.

3.3. *Discussion*

We precede the discussion of the results with some fundamental information about vertical boundary layers in rotating flow. Usually for flow in a rotating container at small Ekman numbers, $E \ll 1$, the transition region between the interior inviscid flow and the vertical wall can asymptotically be divided into two viscous boundary layers, one inside the other. The thinner $O(E^{\frac{1}{3}})$ layer is adjacent to the wall and embedded in the thicker $O(E^{\frac{1}{4}})$ layer. The main physical difference between the two is that in the $E^{\frac{1}{4}}$ layer viscous forces are weaker so that the restoring effect of the Coriolis force on columnar fluid elements is large enough to prevent any vertical variation of the horizontal velocity components, whereas a weak linear variation of w is still possible. To fulfil the complete viscous boundary conditions, a much larger deformation of fluid elements is required, and this is provided by the more viscous $E^{\frac{1}{3}}$ layer, which also redistributes flow from the horizontal Ekman boundary layers to the interior. (For details see e.g. Barcilon 1967 and Greenspan 1968, p. 97.) In our case the channel is assumed narrow enough for the $O(E^{\frac{1}{3}})$ layers at the walls to overlap and no $O(E^{\frac{1}{4}})$ layer is present. However, as the non-dimensional channel width, $2a$, is increased the $O(E^{\frac{1}{3}})$ layers adjacent to the walls tend to be separated by a quasi-$E^{\frac{1}{4}}$ layer in the centre of the channel, in which the horizontal velocity components are almost independent of the vertical coordinate.

Numerical summation of the series solution has been performed for two particular flow cases. The source–sink distribution is in both cases independent of the azimuthal coordinate. This means that the modification of the flow, compared to its axisymmetric counterpart, is only due to the insertion of radial barriers. In the first case the source–sink distribution on the vertical walls, $U_{\pm}$, is zero and the velocities at the horizontal walls are such as to necessitate a radial transport of fluid in the region between the inlets and outlets. In the second case, part, or all of the fluid which is injected at the lower horizontal wall is ejected over a narrow band running along the outer vertical wall. In some, but not all, regards this case is believed similar to the flow in one of the chambers of the actual device. Apart from the fact that the no-slip conditions at the slot do not hold in the actual device, the most doubtful feature of the calculation is probably that the distribution of the radial velocity over the slot – especially in the azimuthal distribution – need not be uniform as assumed. In particular there might also be a significant radial flow through the real slot in the boundary layers at the meridional barriers. To this end, then, we have to be content with geometric and qualitative similarity to the complete flow. The second case is complemented with a study of the trajectories of sedimenting particles.

The flow field has been visualized in several ways: projections of the velocity vectors at selected points (figure 9), contour lines of the velocity components in some planes parallel to the coordinate surfaces (figures 11, 12, 14) and streamlines (figures 10, 13). In all graphs the width of the channel is exaggerated and the cylindrical geometry is not shown.

It is worth mentioning first that when the inlet and outlet conditions are independent of the azimuthal coordinate, as for the cases presented here, it follows from the analysis (see the Appendix) that the radial velocity outside the barrier layers is also independent of s, not withstanding that the flow is fully three-dimensional.

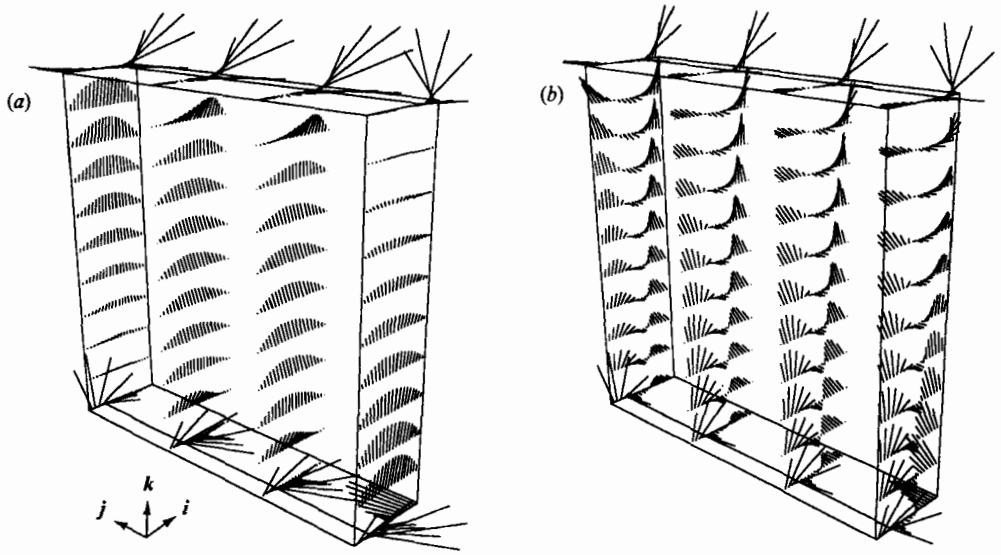

FIGURE 9. Projection of the velocity vector $(\bar{u}, v, w)$ at selected points in an azimuthally blocked channel without a slot for (a) $a = 1$, (b) $a = 3$; $R\Theta = 1$.

A sample of results for the first case are presented in figures 9 and 10 for different values of $a = d/E^{\frac{1}{3}}$. The fluid is injected along the innermost quarter of the lower wall with a parabolic velocity profile and ejected similarly along the outermost quarter of the upper wall. In a very narrow channel, $a \leqslant 0.5$, theory and computation show that the flow almost immediately adjusts to a vertical Poiseuille-like flow. As is the case in axisymetric channels (Barcilon & Berg 1971), radial transport appears within the very short distance of about $H' 2a^3/(\lambda_0^{\mathrm{as}})^3 \sim (d')^3\Omega'/(4\nu')$, close to the inlets and outlets. Away from these regions the radial and azimuthal velocity components are close to zero. The barriers thus have a minor effect on the flow.

For larger values of a, e.g. $a = 1$ in figures 9(a) and 10(a), when the channel width is of the order of the vertical $E^{\frac{1}{3}}$ layers, radial transport occurs in extended regions around the horizontal walls. Owing to the action of the Coriolis force, the fluid here flows in the direction opposite to the rotation, towards the forward-facing meridional barrier. Fluid approaching the barrier is partly forced upwards by the pressure gradient. In the middle of the channel the radial transport is not so pronounced. The azimuthal pressure gradient, supported by the meridional barriers, here forces fluid towards the backward-facing barrier, the azimuthal Coriolis acceleration now being of less importance. Some of the fluid meeting the barriers is turned in the opposite, azimuthal, flow direction by the boundary layers. Close to the inlets and outlets the radial transport in these layers is outwards, whereas in the middle region the transport is inwards.

If the channel is wide enough, e.g. $a = 3$ in figures 9(b) and 10(b), the $O(E^{\frac{1}{3}})$ vertical shear layers tend to be separated from each other. Through the action of these layers, the radial transport between them is almost uniformly distributed along the channel. Vertical flow is more or less restricted to the near-wall regions which supply/withdraw fluid radially to/from the central region between the walls. In the central region the accentuated Coriolis force due to the radial transport induces an azimuthal motion towards the forward-facing barrier. Fluid meeting the barrier is turned in the opposite flow direction into one of the near-wall shear layers. The

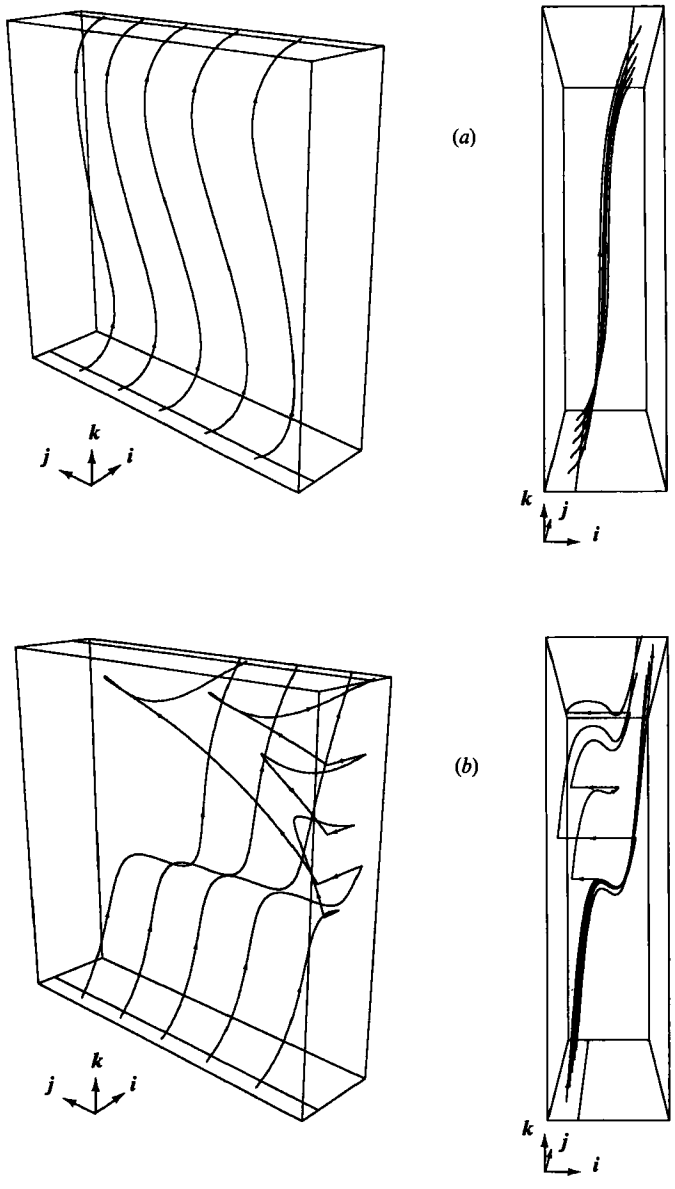

FIGURE 10. Streamlines originating at different azimuthal positions of the inlet in an azimuthally blocked channel without a slot for (*a*) $a = 1$, (*b*) $a = 3$; $R\Theta = 1$. The view direction is from behind the forward-facing barrier behind the inner vertical wall (left) and from behind the forward-facing barrier (right).

streamlines in figure 10(*b*) show that fluid interacting with the barrier layers follows very complicated paths through the channel.

Even if radial transport locally is present at each vertical position in the boundary layers at the barriers, there is in this case no vertically averaged net transport in either of these layers.

The second case is presented in figures 11–13. The flow is here injected over the entire lower wall in the form of a Poiseuille flow and ejected uniformly over a band

$$\xi = a, \quad |z| \leqslant L, \quad |s| \leqslant R\Theta$$

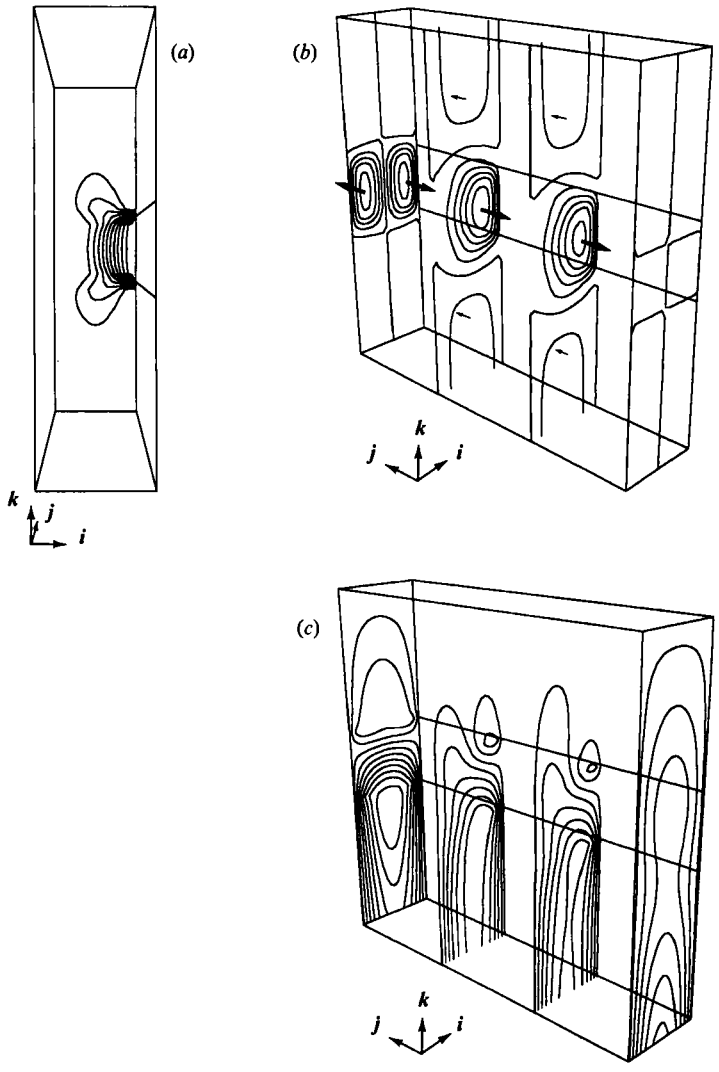

FIGURE 11. Flow in an azimuthally blocked channel when all the fluid is ejected through the slot for $a = 1$, $R\Theta = 1$, $L = 0.2$, showing levels of constant (*a*) $\bar{u}$ in a meridional cut:

$$\bar{u} = 0.45 + (i-1)\ 0.454, \quad i = 1, 2, \ldots, 10;$$

(*b*) v in four meridional cuts at $s = -1.0, -0.4, 0.3, 1.0$: $v = -1.0 + (i-1)\ 0.20$, $i = 1, 2, \ldots, 10$ (the arrows indicate the azimuthal flow direction); (*c*) w in the same meridional cuts: $w = -0.44 + (i-1)\ 0.264$, $i = 1, 2, \ldots, 10$.

at the outer wall. In this case we keep the total flux constant for the different widths of the channel.

For very narrow channels radial transport occurs only in a region localized across the channel, level with the radial outlet. The azimuthal deflection of streamlines is small.

In wider channels, e.g. $a = 1$ in figures 11 and 13(*a*), the region of radial transport is extended. As discussed in the first case, fluid in regions with a pronounced radial transport is forced towards the forward-facing barrier whereas in other regions the fluid tends to flow in the opposite, azimuthal, direction. At the backward-facing

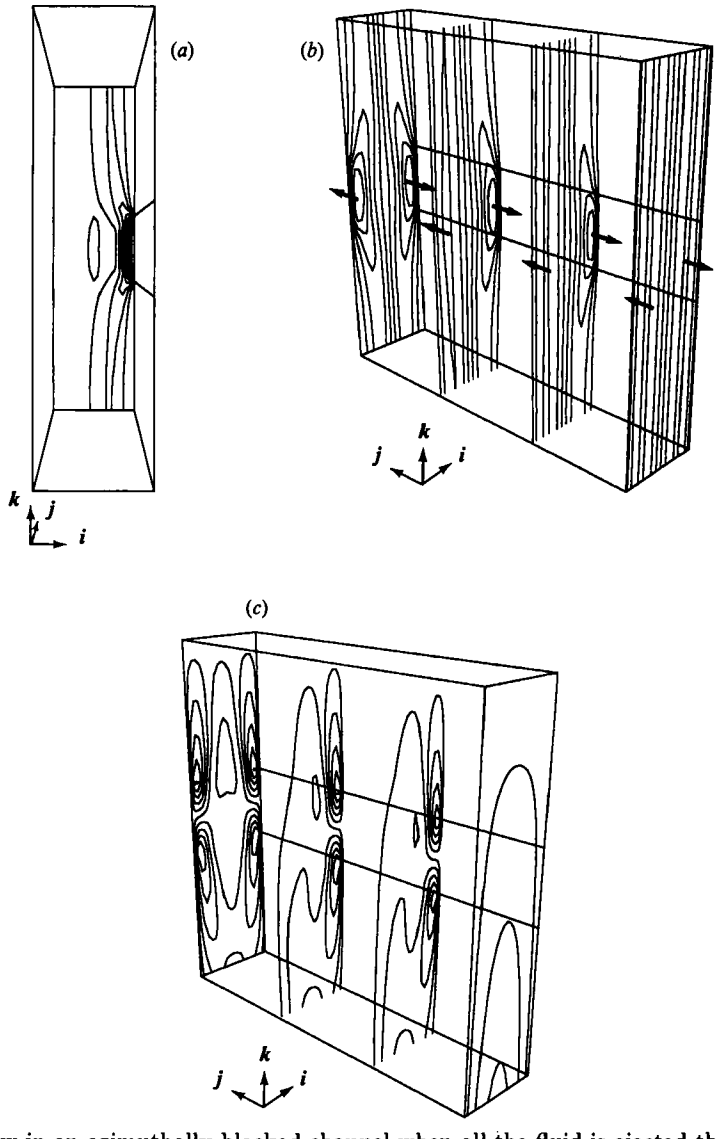

FIGURE 12. Flow in an azimuthally blocked channel when all the fluid is ejected through the slot for $a = 3$, $R\Theta = 1$, $L = 0.2$, showing levels of constant (*a*) $\bar{u}$ in a meridional cut:

$$\bar{u} = 0.45 + (i-1)\,0.454, \quad i = 1, 2, \ldots, 10;$$

(*b*) v in four meridional cuts at $s = -1.0, -0.4, 0.3, 1.0$: $v = -1.31 + (i-1)\,0.291$, $i = 1, 2, \ldots, 10$ (the arrows indicate the azimuthal flow direction; (*c*) w in the same meridional cuts: $w = -0.82 + (i-1)\,0.182$.

barrier, turn around of fluid through the boundary layer takes place whereas this effect is not so strong at the forward-facing barrier.

For cases with separated $E^{\frac{1}{3}}$ layers and a uniformly distributed radial transport in the middle between the vertical walls, as is the tendency for $a = 3$ in figures 12 and 13(*b*), azimuthal motion is dominated by a circulating flow in horizontal planes. The strongest radial motion, appearing next to the wall with the outlet (figure 12*a*), induces flow towards the forward-facing barrier which extends along the whole channel height (figure 12*b*). The fluid is turned by the barrier layer and flows back

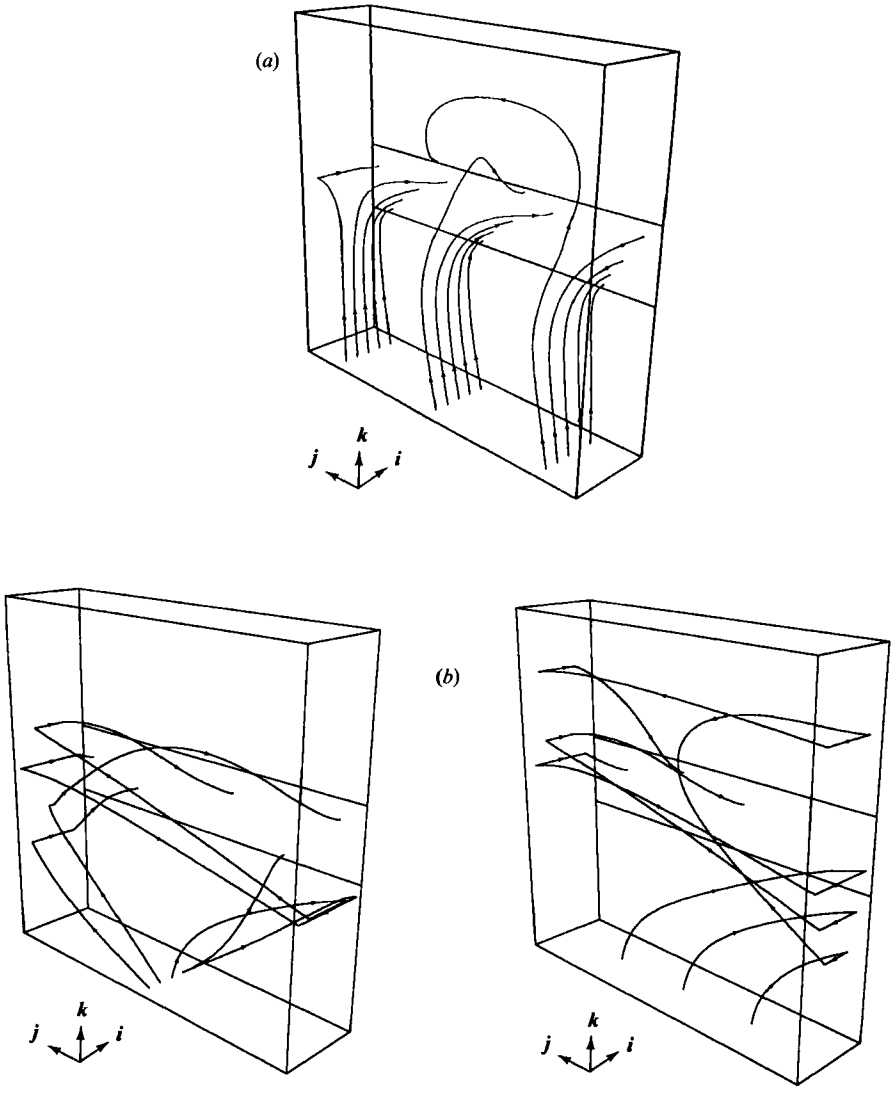

FIGURE 13. Streamlines in an azimuthally blocked channel when all the fluid is ejected through the slot for (a) $a = 1$, originating at different positions over the inlet; (b) $a = 3$, originating along a meridional line at $s = 0$ and an azimuthal line at $\xi = 0$ (right); $R\Theta = 1$, $L = 0.2$.

towards the backward-facing barrier along the opposite wall. The boundary-layer flow at the barriers is thus in opposite directions: outwards at the backward-facing and inwards at the forward-facing barrier. However, the global net radial barrier flow is zero for this case too.

The range of validity in $a = d/E^{\frac{1}{3}}$ of the asymptotic analysis depends in each specific case on the Ekman number E. The Ekman-layer suction, which was neglected in the approximate boundary condition (3.21), is of order $a^2 E^{\frac{1}{3}}$ for large values of a. If one takes $a \sim E^{-\frac{1}{12}}$, which is equivalent to a channel width $d' \sim H'E'^{\frac{1}{4}}$, Ekman-layer suction is of the same order of magnitude as the injection velocity. Part of the radial transport would then take place via the Ekman layers. Inclusion of Ekman-layer suction in the analysis would give a solution uniformly valid for channel widths up to $\sim H'E'^{\frac{1}{4}}$. It has also been assumed that the Ekman layers are

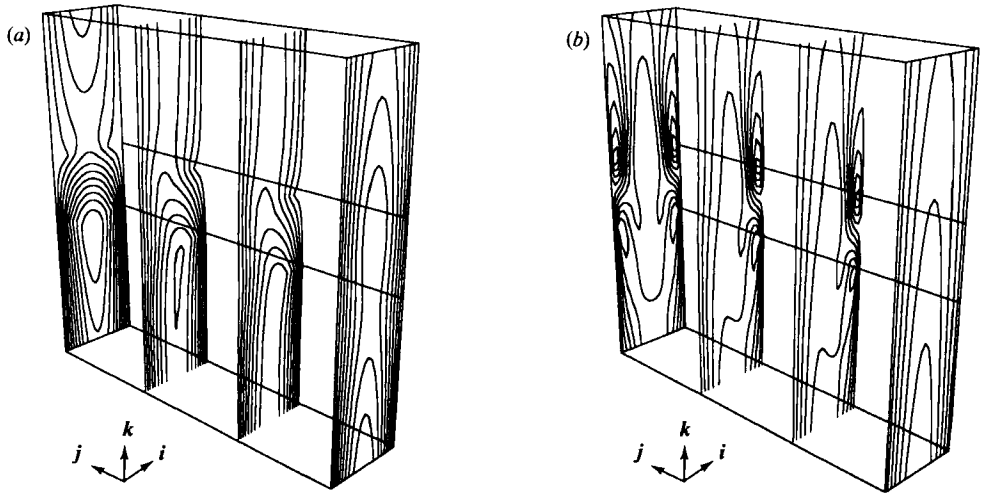

FIGURE 14. Flow in an azimuthally blocked channel when only half the flux is ejected through the slot showing levels of constant vertical velocity for (*a*) $a = 1$, $w = 0.17 + (i-1)\,0.169$, $i = 1, 2, \ldots, 10$; (*b*) $a = 3$, $w = -0.28 + (i-1)\,0.0873$, $i = 1, 2, \ldots, 10$; $R\Theta = 1$, $L = 0.2$.

thin compared to any lengthscales of the flow field. For small values of a this requires $E^{\frac{1}{2}} \ll a^3$. Therefore the range of validity in a,

$$E^{\frac{1}{6}} \ll a \ll E^{-\frac{1}{12}},$$

can be rather narrow in applications where $E^{\frac{1}{12}}$ is not truly small.

Finally we investigate the ability of the device to sort particles by settling in analogy with the axisymmetric case studied in §2. In order to do that we add a vertical Poiseuille flow to the flow field of case two in the previous paragraphs, and thus obtain a flow where only part of the injected fluid is diverted out through the slot in the vertical wall. We trace particles from different positions over the inlet and in channels of two different widths corresponding to $a = 1$ and $a = 3$ respectively. The settling velocity of the particles is chosen at the value given by (1.8) which, according to the kinematic theory, is the lowest settling velocity for which all injected particles pass through the slot for a given flow rate. In scaled, non-dimensional form (1.8) yields

$$\bar{U}_s = \gamma \frac{\bar{Q}}{1+L}, \tag{3.23}$$

where $\bar{Q} = Q/E^{\frac{1}{3}}$ is the scaled flux per unit length into the channel at the lower horizontal wall and γ is the fraction not led through the slot.

Contour lines of the vertical velocity component for the case $a = 1$ are shown in figure 14(*a*). Half of the injected fluid is here diverted out through the slot. One can only just see very small regions of reversed flow on the downstream side of the slot in this case. Particle paths originating at the inner vertical wall are shown to the left in figure 15(*a*). All particles shown settle only slightly above the far edge of the slot. Particles released along the centre of the inlet, as shown to the right in figure 15(*a*), escape as expected through the slot. There are thus no dramatic discrepancies with the kinematic theory, which predicts all particles with settling velocity according to (3.23) to pass through the slot.

Figure 14(*b*) shows the contour lines of the vertical velocity in the wider channel. Here the vertical throughflow cannot prevent a flow reversal on the downstream side

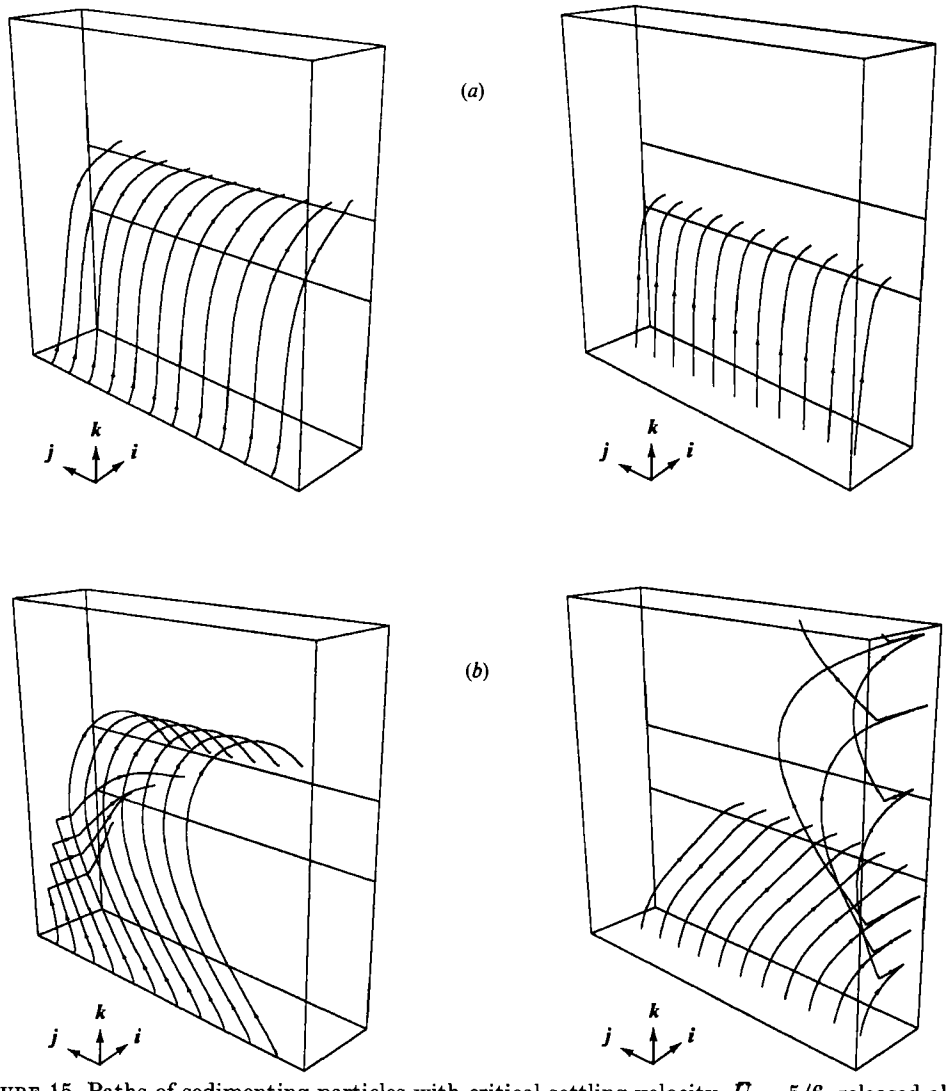

FIGURE 15. Paths of sedimenting particles with critical settling velocity, $\bar{U}_s = 5/6$, released along the inner vertical wall of the inlet (left) and along the centre of the inlet (right) for the flow cases shown in figure 14: (*a*) $a = 1$, (*b*) $a = 3$; $R\Theta = 1$, $L = 0.2$.

of the slot. Particles released at the inner vertical wall of the inlet, as shown to the left in figure 15 (*b*), are initially caught by the main upward flow and also follow the azimuthal stream towards the backward-facing barrier. Reaching the outer part of the channel and after a detour in the upper part, the particles follow the opposite azimuthal stream and are finally directed towards the slot in the region with vertical flow reversal. Most of the particles settle a small distance above the slot edge. Some particles, though, are dragged with the azimuthal stream into the barrier boundary layer and experience a sudden and very rapid radial transport as they are ejected again almost instantaneously at another more outward position. These particles manage to escape through the slot and may even settle on the upstream side of it. Particles released along the centre of the inlet are shown to the right in figure 15(*b*). These particles are caught by the azimuthal stream in the outer part of the channel, directed towards the forward-facing barrier. To a large extent they do escape through

the slot but some of them are captured by the azimuthal flow into the barrier boundary layer. Here, at the forward-facing barrier, the radial transport is inwards and particles are ejected again from the barrier layer at a more inward position. Then, following the azimuthal stream away from the forward-facing barrier and the upward main stream, these particles sediment outwards again but are never even close to passing through the slot. Instead, as can be seen in figure 15(*b*), the particles are again captured by the azimuthal stream into the forward-facing barrier where they experience an additional inward transport. The behaviour is then repeated until the particles are finally carried out through the top outlet.

It should be mentioned that the wash fluid case, discussed in the introduction and treated in §2.2 for the axisymmetric configuration, is only naïvely described by the three-dimensional model used here. Since no fluid is ejected through the wall in this case the inlet Poiseuille profile away from the barrier layers extends unaffected through the whole channel. The barriers are thus without consequence and the kinematic formula for the critical particle settling velocity will be trivially satisfied.

We have seen then, from the simulations for the wider channel, that the particles do not behave at all as expected from the kinematic theory. Firstly, owing to the outward radial flow at the backward-facing barrier, particles with significantly smaller settling velocity than that given by (3.42) can escape through the slot. Secondly, the inward radial flow at the forward-facing barrier prevents some particles from escaping through the slot that were predicted to do so according to the kinematic theory. Therefore, unless the channel is narrow enough, an azimuthally blocked device drastically decreased the ability to sort particles of different settling velocities. One should bear in mind though that these conclusions rest on the assumptions of a simplified model of the three-dimensional flow through a slot as previously discussed in the beginning of this section.

4. Experiment

An important objective is the development of an ultra centrifuge that can separate and fractionate the smallest biological factors – proteins, viruses, antibodies, vaccines etc. – in a truly continuous manner that does not involve stopping the machine as an intrinsic part of the process. A centrifuge to size and sort very much larger particles would also have many technological applications. As the first step to this end, an exploratory experiment was undertaken in order to demonstrate the feasibility of the centrifugal spectrometer and to assess and to verify theoretical models, conclusions and predictions.

A low-speed, two-stage centrifuge, figure 16, was constructed to fractionate, in the manner described earlier, a mixture of two sizes of polystyrene particles with diameters of about 190 and 380 μm respectively. The fluid consisted of water and a water-miscible oil, Ucon 5100HB which enables the relative density difference between solid and fluid, ϵ, to be set fairly precisely in the interval $0.002 < \epsilon < 0.005$. The physical scales, table 1, were chosen to give dimensionless parameters for a simulation with a low-velocity machine where the vertical shear layers were each approximately the channel width in thickness. The flow rate was controlled by setting the exit valves, the flux and/or the rotation rate. In most of the early runs, the machine was placed in a somewhat conservative mode of operation, with the flow set at 75% of the maximum theoretical value, since a proof of feasibility was the main objective. No attempt to date has been made to determine optimal running conditions.

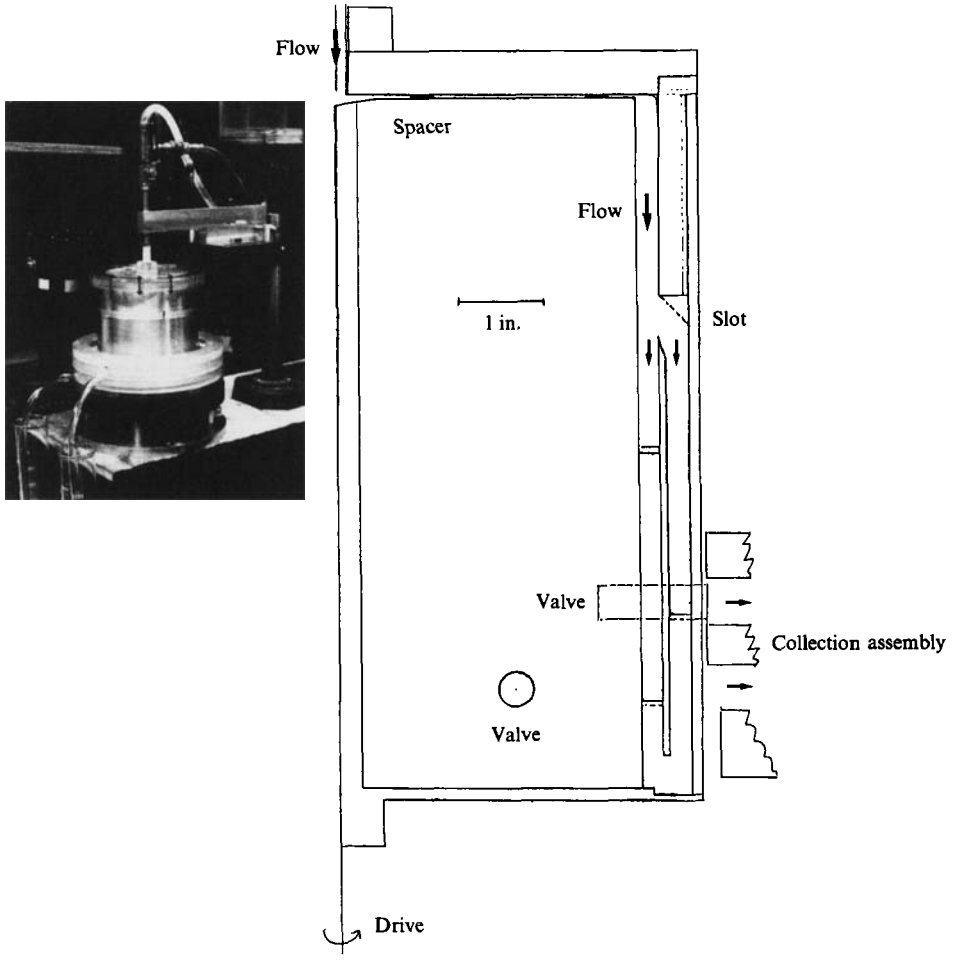

FIGURE 16. A schematic of the centrifuge and (photograph) the early experimental set-up with collection assembly in place.

In practice, the assumption that particles slip or roll along a vertical wall is sometimes difficult to achieve, especially with polymethymethacrylate (PMMA) particles in glycerine and water. Of course, it would have been preferable at the outset to have slanted channels, in order to permit the centrifugal force to move the sediment directly, but the cost of fabrication proved excessive. As an alternative, and as a simulation of the more desirable configuration, the apparatus was operated upside-down, so to speak, which allowed the small gravitational force (measured by the Froude number) to assist in moving particles at the wall. The difficulties were essentially eliminated this way; gravity could also be easily added to the numerical model.

In these experiments, a measured quantity of large, roughly screened particles (350–425 μm) were slowly introduced into the flow by a gravity feed and the output from each channel was carefully collected and weighed. At the prevailing conditions, all these particles should have passed through the slot into the outer channel but size or density dispersity alone, among several other sources of error, made this impossible to achieve. However, it did prove relatively easy to separate and collect 95% or better of the dispersed phase, i.e. a loss of 50 or less particles per thousand

	Ucon oil/H_2O 40/60	Description
r	8.7313	radius (cm)
H	20	height (cm)
L	6.826	stage length (cm)
Ω	40	rotation rate (s^{-1})
ϵ	0.0030	relative density difference
a_1	0.0075	small particle radius (cm)
a_1	0.0175	large particle radius (cm)
ν	0.38	kinematic viscosity (cm^2/s)
F_r	0.0702	Froude number
E	2.375×10^{-5}	Ekman number
δE	0.0975	Ekman boundary-layer thickness (cm)
δV	0.5749	vertical shear-layer thickness (cm)
l	0.635	plate separation distance (cm)
g	0.05	flow cut
t_1	351.0213	settling time, small particle (s)
t_2	64.4733	settling time, large particle (s)
W	0.2044	max channel velocity (cm/s)
Q	7.1205	flow rate (cm^3/s)
R_p	0.0094	particle Reynolds number
R_c	0.03416	channel Reynolds number

TABLE 1. Design parameters

to the inner channel. On occasion the machine ran almost perfectly; figure 17 is a photo of efflux from each channel in one such case.

The major experimental problem is the oil/water composition which is not a true mixture but is more accurately described as a weak association. It seems very easy to break the mixture, the oil degrades the polystyrene beads and the somewhat unstable bonding between water, oil and plastic produces interesting but unexplained effects which, perhaps, contribute to a puzzling inconsistency. It is, however, easy to control the density difference and yet keep the viscosity at an acceptably high value, requirements otherwise difficult to achieve with polystyrene. Another severe problem is getting test particles that have the same settling velocity. The spectrometer when operational will automatically solve this difficulty but, for the present, particles are carefully sifted to narrow the size range and then floated or sunk in solutions of known densities to eliminate deviations.

In the next and ongoing round of experiments, a number of modifications have been made to remedy the aforementioned difficulties. Greater care has been exercised to select test particles more uniform in size and density. PMMA spheres are now used because the larger density of this plastic, 1.18 g/cm^3, can be matched with that of the preferable mixtures of water/glycerine or ethylene glycol/glycerine. (But PMMA particles, individually and as a sediment, are much more difficult to work with than those of polystyrene.) Less important changes concern the control of the flow, new valves, etc., but a complete discussion of the ongoing experiment will appear later, upon completion. However, one noteworthy result already evident is that, with sufficient care, the loss of particles to the inner channel even in this simple device can consistently be made less than 1.5%, or 15 particles per thousand; 0.5% is neither unusual nor the lowest value attained.

With all the constraints imposed and with the limited resources available so far, the results achieved to date are most encouraging for they demonstrate convincingly

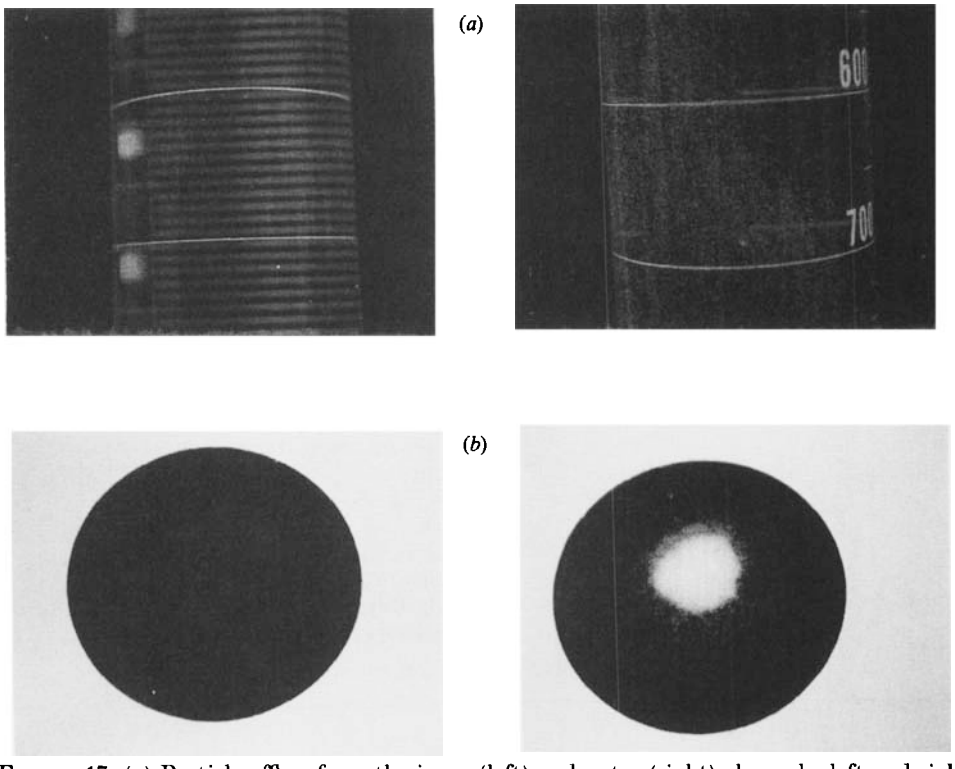

FIGURE 17. (*a*) Particle efflux from the inner (left) and outer (right) channels, left and right respectively. (*b*) Particles collected from each channel.

the practicality of the basic concept and the excellent prospects for developing industrial machines.

5. Conclusions

Rotating flows through narrow axial channels have been considered with emphasis on the application to a device which sorts particles of different sedimentation velocities. This investigation mainly concerns a detailed study of the single-phase flow pattern. An analysis of the axisymmetric flow in two neighbouring channels connected with a slot was done numerically, whereas a linearized model of the three-dimensional flow in a circumferentially blocked channel was studied analytically. Then, with the flow field established, the loci of single particles, small compared to any physical scale of the basic flow and with well-defined settling velocities, were traced through the container.

It was found in both cases that the features of the flow depended strongly on the ratio of the channel width to the thickness of the vertical shear layers. If the shear layers at the axial channel walls overlapped, the flow was only slightly influenced by the Coriolis force, whereas if they were separated and distinct a large, unidirectional and retrograde flow appeared that extended through the entire channel length. The radial motion in the domain was made more uniform as well. In contrast, the azimuthal velocity in the non-symmetric configuration was retrograde only in regions with a pronounced radial transport. Elsewhere the fluid was forced in the same direction as the rotation by the azimuthal pressure gradient supported by the circumferentially blocking barriers.

The validity of a kinematic result obtained for the minimal settling velocity of particles that escapes through a slot in the channel wall was investigated for different flow cases. For overlapping shear layers this critical settling velocity was found to be in satisfactory agreement with the kinematic formula in both flow cases. In wider channels for the axisymmetric motion, a flow reversal on the downstream side of the slot dragged particles of significantly smaller sedimentation velocity through the slot than established by the kinematic theory. However, an extended kinematic formula was found to be valid in which account was taken of the axial extent of the flow reversal region. A similar deleterious effect occurs in the three-dimensional case, which is further augmented by a rapid outward transport in the boundary layer adjacent to the backward-facing meridional barrier. In addition, an inward radial transport adjacent to the forward-facing barrier counteracted the settling of particles in this neighbourhood so that they, in contradiction to the kinematic formula, did not escape through the slot. Thus, the sorting mechanism for wider channels was partly destroyed by the flow at the barriers in the three-dimensional case whereas in the axisymmetric channel a criterion for the sorting mechanism existed in an extended sense dependent on details of the flow field.

Preliminary experimental results show good separation and fractionation of a mixture and, more importantly at this stage, demonstrate the feasibility of the basic concept.

The main conclusions are these:

(*a*) for good separative performance, flow in the channels should be viscously dominated, i.e. the boundary layers must overlap substantially to give as nearly a Poiseuille profile as possible;

(*b*) separation and fractionation are significantly improved using a wash fluid so that only particles (and not fluid) need be diverted between channels;

(*c*) the axisymmetric container and channel configuration work better than one that is sectioned;

(*d*) the concept is feasible.

This work was partially supported by the Swedish Board for Technical Development, the Sweden–America Foundation and the National Science Foundation, Grant number 8519764-DMS.

Appendix. Analysis of the interior solution away from the barriers

The solution is obtained as a superposition of two parts, $\bar{P}_1$ and $\bar{P}_2$, defined respectively by the problems

$$\partial_\xi^6 \bar{P}_1 + 4\,\partial_z^2 \bar{P}_1 = 0; \tag{A 1}$$

$$\partial_\xi \bar{P}_1 = \partial_\xi^4 \bar{P}_1 = \partial_s \bar{P}_1 = 0 \quad \text{at} \quad \xi = \pm a; \tag{A 2a–c}$$

$$\bar{P}_1(\xi = a, z) - \bar{P}_1(\xi = -a, z) = 0 \quad \text{at} \quad s = \pm R\Theta; \tag{A 3}$$

$$\partial_z \bar{P}_1 = \partial_\xi^2 W_\pm(\xi, s), \ (w_1 = W_\pm(\xi, s)) \quad \text{at} \quad z = \pm 1 \tag{A 4a, d}$$

and

$$\partial_\xi^6 \bar{P}_2 + 4\,\partial_z^2 \bar{P}_2 = 0; \tag{A 5}$$

$$\partial_\xi \bar{P}_2 = \partial_\xi^4 \bar{P}_2 = 0, \tag{A 6a, b}$$

$$-\tfrac{1}{2}\partial_s \bar{P}_2 + \tfrac{1}{4}\partial_\xi^3 \bar{P}_2 = U_\pm(s, z) - \tfrac{1}{4}\partial_\xi^3 \bar{P}_1 \quad \text{at} \quad \xi = \pm a; \tag{A 6c, d}$$

$$\bar{P}_2(\xi = a, z) - \bar{P}_2(\xi = -a, z) = 0 \quad \text{at} \quad s = \pm R\Theta; \tag{A 7}$$

$$\partial_z \bar{P}_2 = 0 \quad (w_2 = 0) \quad \text{at} \quad z = \pm 1. \tag{A 8a, d}$$

Observe that the boundary conditions do *not* imply $\bar{u}_1 = 0$ at $\xi = \pm a$. As a consequence an additional source term appears in the boundary conditions, (A 6*c*, *d*), for $\bar{u}_2$ at $\xi = \pm a$. Series solutions for $\bar{P}_1$ and $\bar{P}_2$ are obtained by separation of variables. It can be shown that they are of the form

$$\bar{P}_1 = \bar{P}^P + \bar{P}^Q + \sum_{n=1}^{\infty} \mathscr{X}_n^{\mathrm{s}}(\xi/a)\,(a_n(s)\cosh(k_n z) + b_n(s)\sinh(k_n z)) + \sum_{n=1}^{\infty} \mathscr{X}_n^{\mathrm{as}}(\xi/a)(c_n(s)\cosh(l_n z) + d_n(s)\sinh(l_n z)), \quad \text{(A 9)}$$

with

$$k_n = \frac{1}{2}\left(\frac{\lambda_n^{\mathrm{s}}}{a}\right)^3, \quad l_n = \frac{1}{2}\left(\frac{\lambda_n^{\mathrm{as}}}{a}\right)^3; \quad \bar{P}_2 = \bar{P}^R + \sum_{m=0}^{\infty} [X_m^{\mathrm{s}}(\xi) F_m(s) + X_m^{\mathrm{as}}(\xi) G_m(s)] Z_m(z), \quad \text{(A 10)}$$

with $$Z_m(z) = \sin(\tfrac{1}{2}m\pi)\sin(\tfrac{1}{2}m\pi z) + \cos(\tfrac{1}{2}m\pi)\cos(\tfrac{1}{2}m\pi z),$$

where superscripts s and as denote symmetry and antisymmetry with respect to ξ of the functions $\mathscr{X}_n$ and X_m. The eigenfunctions $\mathscr{X}_n$ with eigenvalues λ_n are adjoints to those studied by Barcilon & Berg (1971) and the X_m are straightforward extensions of functions appearing in unbounded vertical $E^{\frac{1}{3}}$-layers. The coefficients in (A 9) are determined from the boundary conditions (A 4) at the horizontal walls by the use of orthogonality relations for $\mathscr{X}_n$. F_m and G_m in (A 10) are obtained by a system of ordinary differential equations derived from the boundary conditions (A 6*c*) at the vertical walls. $\bar{P}^P$, $\bar{P}^Q$ and $\bar{P}^R$ are particular solutions satisfying at least the no-slip conditions (3.19) and the integral conditions (3.20) at the radial barriers:

$$\bar{P}^P = -3w_m^{\mathrm{s}}\frac{z}{a^2}, \quad \bar{P}^R = -2u_m^{\mathrm{s}}\, s, \quad \text{(A 11}a, b\text{)}$$

$$\bar{P}^Q = -\tfrac{3}{2}w_m^{\mathrm{as}}\frac{z^2}{a^2} + 6w_m^{\mathrm{as}}a^4\left(\frac{\xi^6}{360a^6} - \frac{\xi^4}{24a^4} + 3\frac{\xi^2}{40a^2}\right), \quad \text{(A 11}c\text{)}$$

where

$$w_m^{\mathrm{s}} = \int_{-R\Theta}^{R\Theta}\int_{-a}^{a} \tfrac{1}{2}[W_+ + W_-]\frac{\mathrm{d}\xi}{2a}\frac{\mathrm{d}s}{2R\Theta}, \quad w_m^{\mathrm{as}} = -\int_{-R\Theta}^{R\Theta}\int_{-a}^{a} \tfrac{1}{2}[W_+ - W_-]\frac{\mathrm{d}\xi}{2a}\frac{\mathrm{d}s}{2R\Theta}, \quad \text{(A 12}a, b\text{)}$$

$$u_m^{\mathrm{s}} = \int_{-R\Theta}^{R\Theta}\int_{-1}^{1} (\tfrac{1}{2}[U_+ + U_-] - \tfrac{1}{2}[\bar{u}_1(\xi = a) + \bar{u}_1(\xi = -a)])\frac{\mathrm{d}z}{2}\frac{\mathrm{d}s}{2R\Theta}. \quad \text{(A 12}c\text{)}$$

The corresponding velocity components are

$$\bar{u}^P = 0, \quad v^P = 0, \quad w^P = \tfrac{3}{2}w_m^{\mathrm{s}}\left(1 - \frac{\xi^2}{a^2}\right), \quad \text{(A 13}a\text{–}c\text{)}$$

$$\bar{u}^R = u_m^{\mathrm{s}}, \quad v^R = 0, \quad w^R = 0, \quad \text{(A 14}a\text{–}c\text{)}$$

$$\bar{u}^Q = -\frac{w_m^{\mathrm{as}}}{2}\xi\left(3 - \frac{\xi^2}{a^2}\right), \quad v^Q = 3w_m^{\mathrm{as}}a^3\left(\frac{\xi^5}{60a^5} - \frac{\xi^3}{6a^3} + \frac{3\xi}{20a}\right), \quad \text{(A 15}a, b\text{)}$$

$$w^Q = \tfrac{3}{2}w_{\mathrm{m}}^{\mathrm{as}}\left(1 - \frac{\xi^2}{a^2}\right)z. \quad \text{(A 15}c\text{)}$$

$\bar{P}^P$ thus represent a two-dimensional vertical Poiseuille flow which accounts for a net vertical mean flow w_m^s, and $\bar{P}^R$ represent a uniform radial velocity u_m^s which takes care of the net radial mean flow across $\xi = 0$ not accounted for by $\bar{u}_1$. The third particular solution is a source–sink flow with uniform radial inflow over the vertical walls and an azimuthally independent outflow at the top and bottom with parabolic velocity profiles. This generates a likewise azimuthally independent azimuthal motion, v^Q, with zero net flux.

Actually a great deal of the flow pattern shown by the streamlines in figure 13*b* can be understood by superposition of the particular solutions just mentioned; as the width of the channel, approximately a, is increased, the circulating motion of $v^U \sim w_m^s a^3$ becomes increasingly important compared to other contributions of the flow field.

A fourth particular solution that can be useful in certain cases is given by

$$\bar{P}^S = \frac{K}{2}\frac{z^3-3z}{a^2} - \tfrac{3}{2}Kza^4\left(\frac{\xi^6}{90a^6} - \frac{\xi^4}{6a^4} + 3\frac{\xi^2}{10a^2} - \frac{631}{20475}\right), \tag{A 16}$$

$$\bar{u}^S = \frac{K}{2}z\xi\left(3-\frac{\xi^2}{a^2}\right), \quad v^S = -3Kza^3\left(\frac{\xi^5}{60a^5} - \frac{\xi^3}{6a^3} + \frac{3\xi}{20a}\right), \tag{A 17a, b}$$

$$w^S = \tfrac{3}{4}K\left(1-\frac{\xi^2}{a^2}\right)(1-z^2) + \tfrac{3}{2}Ka^6\left(\frac{1-(\xi/a)^8}{5040} - \frac{1-(\xi/a)^6}{180} + \frac{1-(\xi/a)^4}{40} - 631\frac{1-(\xi/a)^2}{40950}\right), \tag{A 17c}$$

where K is an arbitrary constant. This is also an azimuthally independent flow where the radial flow over the vertical boundaries has a dipole character with inflow in the lower half and outflow in the upper half of the channel. The azimuthal flow is similar to that of the third particular solution but is here in opposite directions in the upper and lower halves of the channel. There is no net vertical transport of fluid across the horizontal boundaries from this solution.

Formal solutions for $\bar{P}_1$ and $\bar{P}_2$ with arbitrary $U_\pm$ and $W_\pm$ have been obtained and will be presented elsewhere. In cases for which $U_\pm$ and $W_\pm$ are independent of the azimuthal coordinate, s, it follows directly from (A 1) and (A 2–A 4) that $\bar{P}_1$, and the corresponding velocity components also are independent of s. However, the solution for $\bar{P}_2$ depends on s even if the source term of the non-homogeneous boundary condition (A 6c) does not. For the radial velocity $\bar{u}_2$, though, we get from (3.17a) and (A 10), after some analysis, the generally valid formula

$$\bar{u}_2 = \bar{u}^R + \tfrac{1}{2}f_0(s) + \tfrac{1}{2}X_0^{as}(\xi)\,g_0(s) + \sum_{m=1}^{\infty}\left[X_m^s(\xi)f_m(s) + X_m^{as}(\xi)\,g_m(s)\right]Z_m(z), \tag{A 18}$$

where $f_m(s)$ and $g_m(s)$ are defined by

$$f_m(s) = \frac{1}{X_m^s(a)}\int_{-1}^{1} U^s(s,z)\,Z_m\,\mathrm{d}z, \quad g_m(s) = \frac{1}{X_m^{as}(a)}\int_{-1}^{1} U^{as}(s,z)\,Z_m\,\mathrm{d}z,$$

and where

$$U^s(s,z) = \tfrac{1}{2}(U_+ + U_-) - \tfrac{1}{2}[\bar{u}_1(\xi = a) + \bar{u}_1(\xi = -a)] - \bar{u}^R,$$

$$U^{as}(s,z) = \tfrac{1}{2}(U_+ + U_-) - \tfrac{1}{2}[\bar{u}_1(\xi = a) - \bar{u}_1(\xi = -a)].$$

Therefore, if $U_\pm$ and $W_\pm$ are independent of s and consequently also f_m and g_m, (A 18) implies that $\bar{u}_2$ is indeed independent of the azimuthal coordinate too.

Another interesting quantity is the part of the net radial flow across $\xi = 0$ that takes place in the boundary layers at the meridional barriers. By direct calculation one obtains for the net azimuthal flow, $\bar{Q}_{\mathrm{bl}}$, into the *inner half* of the respective barrier layers:

$$\bar{Q}_{\mathrm{bl}}(s = \pm R\Theta) = \mp\frac{13}{60} w_m^{\mathrm{as}} a^4 \pm \sum_{n=1}^{\infty} a_n(s = \pm R\Theta)\, \mathscr{X}_n^{\mathrm{s}}(0) \frac{\sinh(k_n)}{k_n}, \quad \text{(A 19}a, b\text{)}$$

which must equal the boundary-layer contributions of the net radial flux across $\xi = 0$. The first term in (A 19) is due to the third particular solution and has opposite sign in the two layers. Therefore this flow does not contribute to the global net flux in the radial direction. The remaining part is solely due to the series solution part of $\bar{P}_1$; when, for all n, $a_n\,(s = R\Theta) = a_n(s = -R\Theta) = 0$ there is no net flux in either of the barrier layers from this part. If $a_n(s = R\Theta) = a_n(s = -R\Theta)$ there is no global net flux through the barrier layers. For all the cases presented in §3.3 the latter statement at least is true.

REFERENCES

Amberg, G. & Greenspan, H. P. 1987 Boundary layers in a sectioned centrifuge. *J. Fluid Mech.* **181**, 77–97.

Barcilon, V. 1967 On the motion due to sources and sinks distributed along the vertical boundary of a rotating fluid. *J. Fluid Mech.* **27**, 551–560.

Barcilon, V. & Berg. H. C. 1971 Forced axial flow between rotating concentric cylinders. *J. Fluid Mech.* **47**, 469–479.

Bennetts, D. A. & Jackson, W. D. N. 1974 Source-sink flows in a rotating annulus: a combined laboratory and numerical study. *J. Fluid Mech.* **66**, 689–705.

Dahlkild, A. A. & Greenspan, H. P. 1989 On the flow of a rotating mixture in a sectioned cylinder. *J. Fluid Mech.* **198**, 155–175.

Davis, R. W. & Moore, E. F. 1982 A numerical study of vortex shedding from rectangles. *J. Fluid Mech.* **116**, 475–506.

Greenspan, H. P. 1968 *The Theory of Rotating Fluids.* Cambridge University Press.

Greenspan, H. P. 1989 United States Patent, No. 4,842,738.

Greenspan, H. P. & Ungarish, M. 1985 On the enhancement of centrifugal separation. *J. Fluid Mech.* **157**, 359–373.

Hide, R. 1968 On source–sink flows in a rotating fluid. *J. Fluid Mech.* **32**, 737–764.

Kan, J.. van 1986 A second order accurate pressure-correction method for viscous incompressble flow. *SIAM J. Sci. Statist. Comput.* **7**, 870.

Shaflinger, U., Köppl, A. & Filipczak, G. 1986 Sedimentation in cylindrical centrifuges with compartments. *Ing.-Arch.* **56**, 321.